Groundwater table fluctuations recorded in zonation of microbial siderites from end-Triassic strata

By Weibel, R.[1*], Lindström, S. [1], Pedersen, G. K. [1], Johansson, L. [2] Dybkjær, K. [1], Whitehouse, M. [3], Boyce, A.[4], Leng, M.J.[5]

[1] GEUS, Geological Survey of Denmark and Greenland, Øster Voldgade 10, 1350 Copenhagen K, Denmark.

[2] Department of Geology, Lund University, Sölvegatan 12, 223 62 Lund, Sweden.

[3] Department of Geosciences, Naturhistoriska Riksmuseet, 104 05 Stockholm, Sweden.

[4] NERC Isotope Geosciences Facilities, SUERC, Rankine Avenue, East Kilbride, G75 0QF, UK.

[5] NERC Isotope Geosciences Facilities (Stable Isotope Facility), British Geological Survey, Keyworth, Nottingham, NG12 5GG, UK.

*Corresponding author: Weibel, R., rwh@geus.dk, Phone: +45 51513364

Keywords

Siderite concretions; sphaerosiderite; spheroidal siderite; oxygen and carbon isotopic composition; microbial activity; groundwater fluctuations

Abstract

In a terrestrial Triassic–Jurassic boundary succession of southern Sweden, perfectly zoned sphaerosiderites are restricted to a specific sandy interval deposited during the end-Triassic event. Underlying and overlying this sand interval there are several other types of siderite micromorphologies, i.e. poorly zoned sphaerosiderite, spheroidal (ellipsoid) siderite, spherical siderite and rhombohedral siderite. Siderite overgrowths occur mainly as rhombohedral crystals on perfectly zoned sphaerosiderite and as radiating fibrous crystals on spheroidal siderite. Concretionary sparry, microspar and/or micritic siderite cement postdate all of these micromorphologies. The carbon isotope composition of the siderite measured by conventional mass spectrometry shows the characteristic broad span of data, probably as a result of multiple stages of microbial activity. SIMS (secondary ion mass spectrometry) revealed generally higher $\delta^{13}C$ values for the concretionary cement than the perfectly zoned sphaerosiderite, spheroidal siderite and their overgrowths, which marks a change in the carbon source during burial. All the various siderite morphologies have almost identical oxygen isotope values reflecting the palaeo-groundwater composition. A pedogenic / freshwater origin is supported by the trace element compositions of varying Fe:Mn ratios and low Mg contents. Fluctuating groundwater is the most likely explanation for uniform repeated siderite zones of varying Fe:Mn ratios reflecting alternating physiochemical conditions and hostility to microbial life/activity. Bacterially-mediated siderite precipitation likely incorporated Mn and other metal ions during conditions that are not favourable for the bacteria and continued with Fe-rich siderite precipitation as the physico-chemical conditions changed into optimal conditions again, reflecting the response to groundwater fluctuations.

Introduction

Siderite is a common early diagenetic mineral occurring with a variety of morphologies in different depositional environments. Rhombohedral and spheroidal (ellipsoid-shaped) siderite are known from marine mudstones and sandstones (e.g. Mozley and Carothers 1992; Mortimer et al. 1997; Wilkinson et al. 2000, Weibel et al. 2010), whereas sphaerosiderite (with internal radial and/or concentric zonation) and spherulitic siderite morphologies (with internal radial structures) and nodules/spheres of siderite (without clear internal structures) are commonly of pedogenic origin (e.g. Browne and Kingston 1993; Retallack 1997; Driese et al. 2010; Robinson et al. 2010; Suarez et al. 2010; Rosenau et al. 2013) and are occasionally found in tidal flats (Choi et al. 2003). A morphological change from spherulitic to rhombohedral siderite during diagenesis has recently been suggested by Köhler et al. (2013) and renders the probability of other explanations for the varying siderite morphologies. In a similar way to the changes during burial of marine sediments, the initial microbial mediated fast precipitation may change into rhombohedral growth, as the supply of Fe becomes slower during increased burial of continental deposits. Zonation is common in rhombohedral and spheroidal siderite, and sphaerosiderites are characterized by internal radial-concentric microstructures. Siderite zonation has previously been ascribed to mixing of meteoric and marine waters (Mozley 1989; Choi et al. 2003), diagenetic evolution of freshwater or brackish-marine pore water during burial (Matsumoto and Iijima 1981; Lim et al. 2004), or modification of the original marine pore waters during successive stages of microbial decomposition of organic matter (Mozley and Carothers 1992; Wilkinson et al 2000; Lim et al. 2004). Despite the wide occurrence of sphaerosiderite, little is known of the pedogenetic conditions (physical, chemical and biological) under which they form and when different siderite morphologies are likely to precipitate (Driese et al. 2010). Precipitation of siderite, even within historical time (< 100 years) shows that microbial degradation of organic contaminants can enhance siderite precipitation rate (Driese et al. 2010). Hence, microbial activity in the pedogenic regime may have promoted precipitation of sphaerosiderite. Siderite formation has been interpreted to be microbially mediated in various environments; marine (Mozley and Carothers 1992; Wilkinson et al. 2000), tidal (Choi et al. 2003), and lacustrine (Fisher et

al. 1998). A wide range in carbon isotope composition ($\delta^{13}C$) of spharerosiderites is interpreted to originate from variations in the type of microbial activity in soils (e.g. Robinson et al. 2010), whereas a more narrow range of oxygen isotope compositions ($\delta^{18}O$) is thought to reflect meteoric water compositions (e.g., Ufnar et al. 2004b; Driese et al. 2010; Robinson et al. 2010; Suarez et al. 2010). The latter has therefore been used as a palaeoproxy for the isotope composition of rainfall, primarily during the Cretaceous (Ludvigson et al. 1998; Ufnar et al. 2001, 2002, 2004a, 2004b, 2004c; Suarez et al. 2009, 2010; Robinson et al. 2010).

The end-Triassic event is one of the five largest biotic crises during the Phanerozoic (Bond and Wignall 2014). It is temporally linked to the emplacement of intrusive and extrusive volcanic rocks during the formation of the Central Atlantic Magmatic Province (Schoene et al. 2010; Blackburn et al. 2013), and degassing from this volcanism is generally believed to have played a major part in the extinction scenario (e.g., Hesselbo et al. 2002; Ruhl et al. 2011; Lindström et al. 2012). Organic $\delta^{13}C$ records across the Triassic–Jurassic boundary show large negative perturbations in the carbon cycle interpreted as reflecting input of light carbon from the volcanism or from methane release (e.g. Hesselbo et al. 2002). In the terrestrial realm, physiological responses in fossil plants indicate intense global warming across the Triassic–Jurassic boundary (McElwain et al. 1999). Increased storminess and lightning activity are further indicated by charcoal records showing increased wildfire activity from Greenland, Denmark, Sweden and Poland (Marynowski and Simoneit 2009; Belcher et al. 2010; Petersen and Lindström 2012). Sedimentary records from the Danish Basin indicate increased reworking of palynological material (Lindström et al. 2012), and marked changes in fluvial terrestrial successions in Sweden and Greenland seem to indicate an increased water content in the hydrological cycle across the boundary (Lindström and Erlström 2006; Steinthorsdottir et al. 2012).

Sphaerosiderites and other siderite morphologies have previously been reported from Triassic–Jurassic boundary sediments (Höganäs Formation) in Scania, southern Sweden (Fig. 1; Troedsson 1951; Ahlberg 1994). Troedsson (1951) reported sphaerosiderites from early – middle Rheatian clayey sediments (Vallåkra Member of the Höganäs Formation) in several old cored wells and outcrops in northwest and central Scania,

and concluded that sphaerosiderites were restricted to this particular interval. Here we show that sphaerosiderites also occur within the latest Rhaetian sand and sandstones (Helsingborg Member of the Höganäs Formation), although they are apparently absent from the intermediate part (Bjuv member of the Höganäs Formation) (Fig. 1). The purpose of this study is to find explanations for the different siderite morphologies and contribute to the understanding of sphaerosiderite formation, and its implications regarding Triassic – Jurassic-boundary events. In northwest Scania, southern Sweden, the end-Triassic terrestrial succession is characterized by a pronounced shift in depositional style and in occurrence of various types of authigenic siderite. Mid to late Rhaetian forest mires and confined fluvial channel deposits are completely free of authigenic siderite, whereas the overlying latest Rhaetian unconfined and probably episodic braided river deposits are dominated by siderite concretions and authigenic siderite. In this sense, the Albert-1 core, Norra Albert quarry and the Fleninge No. 266 core (Fig. 2), which together encompass Norian–Hettangian strata, provide excellent opportunities for such investigations as perfectly zoned sphaerosiderite occur juxtaposedwith other siderite morphologies.

Fig. 1: Stratigraphy

Fig. 2: Map

Geological setting

During the Late Triassic – Early Jurassic the Norwegian–Danish Basin was situated on the margin of an epicontinental basin covering NW Europe (e.g. Fischer and Mudge 1998; Nielsen 2003). Southern Sweden was part of the Fennoscandian Border Zone, which is structurally defined by the Sorgenfrei-Tornquist Zone, and marks the transition from the Fennoscandian Shield to the north-east and the gradually deepening (epicontinental) basin towards the south-west (Fig. 1; Liboriussen et al. 1987; Mogensen and Korstgård,

2003; Nielsen 2003). Therefore, minor sea-level changes played a significant role in controlling the lateral facies distribution (Ahlberg et al. 2003). In Scania, the southernmost part of Sweden, typical continental red beds of the Norian Kågeröd Formation, deposited under a semi-arid regime, are succeeded by claystones, sandstones and coals belonging to the Rhaetian-Hettangian Höganäs Formation (Fig. 1). The oldest member of the Höganäs Formation, the Vallåkra Member, consists of variegated smectitic clays and sands which constitute a transition from the underlying red beds of the Kågeröd Formation to the kaolinite-rich underclays, mature sands and coals of the Bjuv Member (Ahlberg et al. 2003). The Norwegian–Danish Basin was transgressed in two steps (indicated on Fig. 1) during the Rhaetian, culminating with a maximum transgression (MFS7) that can be traced all over the Danish part of the Norwegian–Danish Basin (Figs 1 and 3; Nielsen 2003; Lindström and Erlström 2006). The marine transgression reached as far in Scania as the localities Helsingborg and Lunnom, and at Norra Albert an incursion of marine dinoflagellates probably represents marine waters entering the rivers during storm episodes (Fig. 1; Lindström and Erlström 2006). The precursor mires, resulting in the Bjuv Member coals/coaly beds, were formed on a low-relief coast affected by a transgressive event in the mid-late Rhaetian (Petersen et al. 2013). The change from a semi-arid climate during the Norian to more humid conditions during the Rhaetian has been attributed to effects of the marine inundation of the Central European Basin from the Tethys (Ahlberg et al. 2002). Climatic changes at the Triassic–Jurassic boundary that forced supraregional deforestation in NW Europe, (van de Schootbrugge et al. 2009) which severely affected the forest mires (Petersen and Lindström 2012), may have triggered the changes in continental deposits from mire forests and wetlands with confined fluvial channels (Bjuv Member) to braided streams of the Boserup beds (Helsingborg Member) (Lindström et al. 2015). The Boserup beds constitute the basal part of the Helsingborg Member (Sivhed 1984, Troedsson 1951). Some authors have placed the boundary between the Bjuv Member and the Helsingborg Member at the top of coal bed A, i.e. at c. 3 m in Fig. 3A (Sivhed 1984). In the Norra Albert quarry the boundary of the Boserup beds has not been formally defined. In the present paper it is placed at 6 m in Fig. 3A based on sedimentological considerations. The Bjuv Member is characterized by mudstones and coal beds with subordinate sandstones interpreted as fluvial deposits. The overall depositional environment is interpreted as a floodplain. The coal bed A is overlain by carbonaceous mudstone and with strongly deformed sand beds 5.0–6.2 m (Fig. 3A).

This succession comprises thin beds of fine-grained sand with graded bedding separated by mud-drapes. The sand shows ripple-cross-lamination, indistinct lamination and locally parallel bedding. The sedimentary structures suggest episodic, non-channelized deposition of sand in a flood-plain environment. Two phases of soft-sediment deformations are interpreted caused by seismic shocks (Lindström et al. 2015). They are erosionally overlain by the Boserup beds, which are a distinct association of facies dominated by structure less, parallel bedded and trough cross-bedded sand, with several large concretions. The Boserup beds are interpreted as braided stream deposits.

At the Norra Albert quarry and in the Fleninge No. 266 well this terrestrial ecosystem change is marked by a gradual loss of Taxodiacean/Cupressacean gymnosperm pollen (*Perinopollenites elatoides*) from trees that thrived in mires in favour of the enigmatic gymnosperm pollen tetrad *Ricciisporites tuberculatus*, representing an unknown habit, perhaps ruderal / scrubby (Kürschner et al. 2014). A similar shift in dominating pollen-type is recorded in marine sediments (the Stenlille-1 well – see Fig. 2) representing a sediment source-area larger than that of the investigated terrestrial localities (Lindström et al. 2012). In addition, repeated intervals of seismites occur at the Triassic-Jurassic transition at the Norra Albert quarry (Lindström et al. 2015) coinciding with the occurrence of perfectly zoned sphaerosiderite (Fig. 2).

Fig. 3: Sedimentary logs from Norra Albert quarry, Albert-1 and Fleninge No. 266 cores.

Methodology and terminology

The samples comprise outcrop rock samples taken during field work in the Norra Albert quarry 2009 - 2012 and core samples from the Albert-1 and the Fleninge No. 266 wells, which were drilled in 2009 and 1935, respectively. Consequently, the samples from the Fleninge No. 266 well were restricted by the limited remaining core samples.

Petrography was evaluated from polished thin sections using a Zeiss Axioplane for transmitted and reflected light microscopy. Supplementary studies of crystal morphologies, dissolution features and paragenetic relationships were performed on gold coated rock chips mounted on stubs and on carbon coated thin sections using a Phillips® XL 40 scanning electron microscope (SEM) operated with secondary electron detector (SE) and back-scatter detector (BSE), respectively. The SEM was equipped with an energy dispersive X-ray analysis (EDX) system Thermo Nanotrace® 30 mm^2 detector surface window and a Pioneer Voyager® 2.7 10 mm^2 window Si(Li) detector. The electron beam was generated by a tungsten filament operating at 17 kV and 50-70 μA. One sample was partially dissolved in hydrochloric acid heated at 30°C in 2 hours under agitation in order to enhance visibility of growth structures in the SEM.

Bulk samples for X-ray diffraction (XRD) analysis were mounted with random orientation. Samples were scanned on an automated Philips® PW 3710 X-ray diffractometer with automatic divergence slit, using graphite monochromated CuKα radiation. Quantification of major mineral phases based on bulk samples was done by Rietveld analysis of X-ray diffractograms.

Total abundances of the major oxides and several minor elements were analysed by ICP-ES (inductively coupled plasma-emission spectrometry) and the rare earth elements were determined by ICP-MS (inductively coupled plasma-mass spectrometry) at ACME laboratory. The samples were fused by lithium metaborate/ tetraborate and digested in dilute nitric acid. Total S and C were analysed by LECO. The major elements were applied for calculation of mineral abundances.

Quantitative chemical analyses of the carbonates were performed on a JEOL® JXA-8200 electron microprobe operated at an acceleration voltage of 15 kV, a beam current of 8 nA and a spot size of 10 μm. Carbon coated thin section were applied.

Carbon and oxygen isotopes were analysed on bulk rock samples by IRMS (isotope ratio mass spectrometry) and *in situ* by SIMS (secondary ion mass spectrometry) on thin sections. Bulk rock carbon and oxygen isotope analyses using a VG SIRA II dual inlet mass spectrometer were performed on carbon dioxide released from the carbonates after reaction with phosphoric acid at 25°C for 3 hours (calcites) and at 100°C for 96 hours (siderites) at the SUERC facility in the UK. This way the major part of carbon dioxide produced at 25°C will be from calcite, ensuring that the subsequent produced (at 100°C) carbon dioxide was dominantly from siderite. The fractionation factors used were from Friedman and O'Neil (1977) (calcite) and Rosenbaum and Sheppard (1986) (siderite). Carbon and oxygen isotope data ($\delta^{13}C$ and $\delta^{18}O$) are presented in the standard δ notation relative to PDB, Pee Dee Belemnite (Craig 1957). In situ carbon and oxygen isotopes measurements, were performed at the NORDSIM facility, Stockholm, using a CAMECA® IMS1280 large-geometry ion microprobe using a 20 kV, ca. 10 µm Cs^+ primary beam, a low-energy electron-flooding gun to compensate for charge build-up and simultaneous detection in either two Faraday detectors (for ^{16}O and ^{18}O) or a Faraday together with an ion-counting electron multiplier (for ^{12}C and ^{13}C respectively). All analyses were performed in automated chain sequences that regularly interspersed analyses of unknowns with those of standards. Because there is no universally accepted siderite standard we developed our own through the Stable Isotope Facility (SIF) at the BGS using a VG Optima dual inlet mass spectrometer and the Isotope Community Support Facility (ICSF) at SUERC using a VG SIRA II dual inlet mass spectrometer). These two laboratories have slightly different analytical methods but agreed on the preferred value for our principal standard, to which we compare our data. The siderite standard is from Ivigtut cryolite deposits, Ivigttuut, Greenland. It was reacted under vacuum with anhydrous phosphoric acid at a constant 100°C for 96 hours (SIF) and at 70°C for one week (ICSF). The CO_2 liberated was cryogenically separated from water vapour under vacuum and analysed using IRMS. The mineral-gas fractionation factor used for siderite was 1.00881 (derived from Rosenbaum and Sheppard, 1986). The oxygen and carbon isotope composition of the siderite ($\delta^{18}O$ and $\delta^{13}C$) are reported as per mil (‰) deviations of the isotope ratios ($^{18}O/^{16}O$ and $^{13}C/^{12}C$) calculated to the V-PDB scale. The SIF derived value for the siderite standard was –21.97‰ (0.09 1SD) $\delta^{18}O$ and –8.08‰ (0.02 1SD) for $\delta^{13}C$. The ICSF derived value for the siderite standard was –22.13‰ (0.23 1SD) $\delta^{18}O$ and –8.51‰ (0.17 1SD) for $\delta^{13}C$. Consequently,

average values of –22.04‰ (0.17 1SD) for $\delta^{18}O$ and –8.25‰ (0.24 1SD) for $\delta^{13}C$ were achieved when compiling all standard measurements and were applied for correcting the SIMS data.

Results, sedimentology and petrography

Occurrence of siderite in the sediments

At the Norra Albert quarry siderite concretions are confined to the coarse-grained, poorly sorted, fluvial sandstones of the Boserup beds and sporadic siderite cement in the uppermost part of the Bjuv Member (Fig. 3A), whereas their absence is notable in the underlying more clayey floodplain sediments of the Bjuv Member. In general, the siderite concretions (ranging in size from 20 cm – 2 m) are developed preferentially along the stratification (Fig. 4A, 4C and 4D). In some cases, the concretions appear to have initiated locally in the most coarse-grained undulating intervals followed by continued siderite growth into the surrounding finer-grained sand intervals, which cuts the sedimentary structures (Fig. 4E and 4F). In rare cases, petrified wood occurs in the centre of siderite concretions (Fig. 4B).pure siderite occurs. The pure siderite can be either detrital, very early siderite, or a late infilling in the centre of the concretion (cf. Bojanowski et al. 2016). Siderite may comprise a relatively large proportion of the concretions, suggesting that siderite precipitation took place as displacive growth (Fig. 5).

The Albert-1 core (Fig. 3B) shows that authigenic siderite is absent in the Bjuv Member, though present in the underlying Vallåkra Member. Core samples from the Fleninge No. 266 well (Fig. 3C) verify the presence of perfectly zoned sphaerosiderite and other authigenic siderite morphologies in the lower part of the Boserup beds; and confirm that authigenic siderite is absent in the Bjuv Member, though present at the boundary to Vallåkra Member (Fig. 3C).

Fig. 4: Siderite concretions at N Albert quarry

Fig. 5: Calculated mineral abundance

Siderite micromorphology

The siderite micromorphologies are divided into the following types that precipitated in successive order:

1. Zoned sphaerosiderite and spheroidal siderite, which is subdivided into: 1A perfectly zoned sphaerosiderite: 1B poorly zoned sphaerosiderite (and spherulites); and 1C zoned spheroidal siderite.
2. Radial siderite overgrowths, which exhibit variable habits according to their substratum: from mainly rhombohedral on the perfectly zoned sphaerosiderite (A) to preferentially fibrous, when growing on the spheroidal siderite (B).
3. Microcrystalline, anhedral or subhedral, randomly orientated pervasive siderite cement that forms concretionary cements. Rhombohedral single siderite crystals dispersed in the sandstones are considered initial precipitations in 'immature concretions' (compare with Bojanowski et al. 2016).

Zoned sphaerosiderite and spheroidal siderite

Perfectly zoned sphaerosiderite and zoned spheroidal siderite are common in the siderite concretions in a specific interval in the Boserup beds partly coincident with the interval of soft sediment deformation structures (Fig. 3A). Poorly zoned sphaerosiderite generally occurs scattered, though is occasionally abundant in concretions, immediately below this interval, i.e. in the uppermost part of the Bjuv Member (Fig. 3A and 3C). Scattered poorly zoned sphaerosiderites are common in concretions in the overlying Boserup beds (Fig. 3A). Poorly zoned sphaerosiderite occurring in the basal part of the Bjuv Member (Fig. 3C) never encloses detrital grains and are oversized compared with sphaerosiderite in the Bjuv and Helsingborg members, though similar to those occurring in the Vallåkra Member analysed by Troedsson (1951) and

slightly resembling the cemented areas of the Vallåkra Member in the Albert-1 well (AL1-09.28 in Fig. 3B). These oversized sphaerosiderite may not have been formed *in situ* within the Bjuv Member deposits, but probably precipitated in older strata (e.g. Vallakra Member) and were redeposited.

Poorly zoned sphaerosiderite has an inner core surrounded by a rim of rhombohedral or irregular crystals (Fig. 6). Perfectly zoned sphaerosiderite has an inner core of radiating growth (which gives rise to a characteristic extinction pattern) in few to several concentric zones (Fig. 7). The outermost rim of rhombohedral crystals is partly coalescent with the cement filling the shrinkage fracture between the detrital grains and sphaerosiderite. Sphaerosiderite commonly occurs in clusters (Figs 7E and 8B) forming a coccoid morphology (compare Driese et al. 2010). Sphaerosiderite zonation is caused by variation in mineralogy and chemistry. Rhodochrosite zones in sphaerosiderite seem to be more affected by dissolution than siderite (Fig. 8A). Rhodorchrosite abundance of up to 25% of the cement of one concretion is documented by XRD. In other concretions, ankerite dolomite and/or rhodochrosite are occasionally present in XRD detectable amounts. Poorly zoned sphaerosiderite occur with dissolution voids next to poorly zoned sphaerosiderite having a core of increased Ca, Mn and Si contents, suggesting that dissolution preferentially occurred in other carbonate phases and low Fe siderite (Fig. 6B and 6D). Zonation enhanced by weathering in other sphaerosiderites (Fig. 7C) may also originate from other carbonate minerals or incorporation of varying amounts of Ca, Mn (Mg?) and Zn in the siderite structure (Fig. 8A and 8C). Zonation patterns are uniform within concretions, though vary between different concretions (Figs 7D and 8A).

Zoned spheroidal siderite has an inner core of radiating crystals similar to the perfectly zoned sphaerosiderite, and only few but regular spheroidal zones (Fig. 9). The spheroidal siderite has a more uniform size (30 – 80 µm) than the size of the perfectly zoned sphaerosiderite (20 – 350 µm) and the usual size of poorly zoned sphaerosiderite (3 – 170 µm) (Fig. 3).

Overgrowths on siderite morphologies

Perfectly zoned sphaerosiderite is typically surrounded by a rim of rhombohedral siderite crystals (Fig. 7).The outermost rim of rhombohedral crystals is partly coalescent with fracture-healing cement between the detrital grains and perfectly zoned sphaerosiderite (Fig. 7A, 7B and 7D). The overgrowths on the zoned spheroidal siderite preferentially consist of radiating crystals (Fig. 9A).

Concretionary siderite cement

Sparry, microspar or micritic siderite cement encloses perfectly and poorly zoned sphaerosiderite and spheroidal siderite to form concretions. Dispersed rhombohedral siderite and poorly zoned sphaerosiderite characterise the weakly-cemented sandstones in the lower part of the exposed Boserup beds at Norra Albert, whereas the upper exposed part of the Boserup beds have concretions with poorly zoned sphaerosiderite (Fig. 3A). The dispersed siderite occurs preferentially in the most coarse-grained intervals.

Siderite in relation to other minerals

Siderite is typically non-corrosive against detrital grains, which support a displacive growth of the siderite cement. However, siderite crystals and spheres grow along cleavage planes in mica and feldspar and more rarely in secondary porosity after feldspar and altered Fe-Ti oxides. Few authigenic phases predate siderite. Rare pyrite, enclosing micro-spheres of siderite, is enclosed in the centre of sphaerosiderite so pyrite mainly predates siderite. Kaolinite (crystal sizes: 2 – 4 µm) occur enclosed in rhombohedral siderite and partly dissolved feldspar, and are enclosed in sparry siderite cement. Other authigenic phases, such as kaolinite (crystal size: 5 – 10 µm), anatase and possibly quartz, occur in the central dissolution voids after poorly zoned sphaerosiderite (Fig. 6C) and consequently postdate siderite. The authigenic origin of quartz is suggested from its euhedral shape and from the ubiquitous initial quartz overgrowths on detrital quartz, in general.

Alteration products, such as manganese oxides/hydroxides and iron-oxides/hydroxides, are common in most sandstones. Iron-oxide/hydroxides (hematite in one sample) occur in altered zones of sphaerosiderite and spheroidal siderite and as alteration rims around rhombohedral siderite. Manganese oxides/hydroxides occur as authigenic rims around detrital and authigenic phases, though without any specific petrographic relationship to the chemistry of the carbonate phases.

Fig. 6: Poorly zoned sphaerosiderites (spherulites, spherulitic siderite)

Fig. 7: Perfectly zoned sphaerosiderites

Fig. 8: Varieties of zoned sphaerosiderites

Fig. 9: Spheroidal siderite (pseudomorphs after organic matter?)

Chemical composition

Low CaMg siderites (Fig. 8) dominate all siderite morphologies with typically < 5 % $CaCO_3$ and < 3 % $MgCO_3$. Maximum 11 % $MgCO_3$ (sample 516816), 10 % $CaCO_3$ (sample 516814) and up to 0.9 % $ZnCO_3$ occur in some samples. $MnCO_3$ is more common with up to 10 %. Poorly zoned sphaerosiderite has a tendency of slightly higher content of $CaCO_3$, up to 10 %, than other siderite micromorphologies. Zoned spheroidal siderite, perfectly zoned sphaerosiderite and their overgrowths have the highest content of $MnCO_3$, up to 35 % (Fig. 8).

Fig. 10: Chemical composition

Isotope composition

The $\delta^{18}O$ of siderite is mostly unrelated to the siderite morphology, because concretions and weakly cemented sandstones containing perfectly zoned and poorly zoned sphaerosiderite, spheroidal and rhombohedral siderites appear with similar oxygen isotopic compositions (SIMS: –4.7 to –5.1‰ $\delta^{18}O$ and IRMS:–4.8 to –5.3‰ $\delta^{18}O$) (Table 1; Fig. 11). Sphaerosiderite with rhodochrosite zones group together with other perfectly zoned sphaerosiderites (Fig. 11A). Samples containing small rhombohedral siderites, which are more prone to alteration, have relatively lower $\delta^{18}O$ values (down to –7.5‰). One intensively altered sample with even lower values has been left out, as the high amounts of iron-oxide/hydroxides affected the oxygen isotopic composition.

The SIMS measurements show clearly more positive $\delta^{13}C$ values for the concretionary cement (–5.5 to +7.8‰) than for the siderite micromorphologies, such as perfectly zoned sphareosiderite (–17.3 to –2.4‰), spheroidal siderite (–101.1 to –5.1‰) and their overgrowths (–13.0 to +3.0‰) (Fig. 11B). The somewhat wider span in $\delta^{13}C$ values (–17.3 to +7.8‰) for the *in situ* SIMS measurements compared to bulk rock IRMS measurements (–11.6 to +6.0‰ $\delta^{13}C$) is a result of different mixtures of sphaerosiderite and spheroids and concretionary cement in the bulk rock samples.

Fig. 11: Isotopic composition

Table 1. Isotopic composition

Discussion

Microstructural growth pattern

A wide spectrum of siderite morphologies is represented in the Norra Albert quarry. It is remarkable to find perfectly concentrically-zoned sphaerosiderite, spheroidal siderite, rhombohedral siderite and poorly-zoned sphaerosiderite occurring together. Poorly zoned sphaerosiderite could be the precursor to perfectly zoned sphaerosiderite, which forms only under specific conditions.

Poorly-zoned sphaerosiderite and spherulites with central dissolution voids cannot, strictly speaking, be distinguished. Internal dissolution voids in rhombohedral siderite and spherulites may origin from siderite growths around a core of different chemistry or carbonate mineralogy, an episode of crystal poisoning (Wilkinson et al. 2000) or it may be explained by areas ('eyes') of less stability within the spherulites originating from its primary growth pattern (Gránásy et al. 2005). In the latter case no chemical or mineralogical zonation is necessary in order to explain the central instability.

Radiating growth patterns are characteristic of the centre of perfectly zoned sphaerosiderite and spheroidal siderite (Figs 7 and 9), but are more difficult to discern within the spherulites and poorly zoned sphaerosiderites. The growth begins from a nucleus that seems very small in the sphaerosiderite. The constrained spheroidal shape suggests some kind of growth control, possibly of organic origin, for example within spheroidal pollen grains or within stomata of leaf cuticles (compare stomata of leafs of *ginkgoites* or *anomozamites* known from a Rhaetian flora in Scania reported by Pott and McLoughlin (2011)). Siderite precipitation may have started along the inside of the pollen wall as the spore-cell material decayed, or along the guard cells of the open pores of the stomata, with subsequent continued growth inwards towards the centre of the pollen grain/ stomata. As the organic matter degraded, growth of siderite radiating outwards from the original location of the guard cells followed. Other types of organic matter may have acted as

nucleation sites for the sphaerosiderite growth. The growth pattern changes from radial to rhombohedral, as spherulites were enclosed in sparry or rhombohedral siderite, and as rhombohedral crystals rimmed the perfectly zoned sphaerosiderite (Fig. 7C and 7D). This change in growth pattern could reflect biogenically facilitated, radially- and concentrically-zoned siderite, succeeded by a relatively slower precipitation of siderite, beginning with rhombohedral crystals and ending with sparry and/or microsparry cement. A diagenetically-induced change of spherulitic to rhombohedral siderite morphology is advocated by Köhler et al. (2013), but it seems less likely that only the outermost part of the sphaerosiderite and spherulites should be diagenetically altered prior to enclosure in sparry or microsparry siderite cement. In this case, a more reasonable explanation would be continued growth under changed conditions and hence with different precipitation rates, from bacterially-mediated Fe^{3+} reduction to microbial fermentation of organic matter in the methanogenic zone (e.g. Hicks et al. 1996; Ludvigson et al. 1998; Krajewski et al. 2010).

The perfect zonation of sphaerosiderite is so pronounced and systematic (Fig. 7D) that it cannot merely have formed from alteration processes. Rather, the alteration processes have enhanced the visibility of the detailed zonation (Fig. 8A) with *in situ* alteration products of iron-oxide/hydroxide and dissolution voids after less stable phases such as Ca or Mn-rich siderite and rhodochrosite. Dissolution voids begin within the pure rhodochrosite zones rather than in the siderite, so rhodochrosite zones dissolve faster than siderite (Fig. 9A). Rhodochrosite forms under suboxic conditions whereas siderite precipitates under anoxic conditions (Bojanowski et al. 2016), hence rhodochrosite is likely to be more stable under oxidizing conditions. However, dissolution products of rhodochrosite are removed faster from points of dissolution since Mn^{2+} is slightly more soluble than Fe^{2+} (Sholkovitz and Copland 1981). The central part of the spherulites and poorly zoned sphaerosiderites is commonly dissolved; but when present the central part generally has higher contents of Mn, Ca, and occasionally Si. It is therefore probable that the dissolution zones/centres are located where the siderite has incorporated relatively high amounts of Mn and Ca. This would explain the common occurrence of *ex situ* manganese-oxides/hydroxides as alteration rims covering both detrital grains and authigenic phases, though without any petrographic association with siderite or rhodochrosite.

Bacterial mediated perfect zonation?

The growth of sphaerosiderite started on organic or detrital grains and continued in spherical zones around the nuclei as the bacterial colony continued its reduction of Fe and Mn, which reacted with HCO_3^-, liberated from the degradation of organic matter and precipitated as siderite (and rhodochrosite). Spheroidal siderite started as impregnation of voids in organic tissue, for example pollen or stomata, and continued with zonal growth of siderite crystals on the pollen wall or the guard cells and gradually filled the void (Fig. 12). This could explain the uniform size of spheroidal siderite (Fig. 4A). After degradation of the surrounding organic matter, the siderite growth continued outwards with larger radiating crystals, possibly reflecting more slowly sourced iron.

Most investigations of sphaerosiderite record large variations in $\delta^{13}C$ (Table 1; e.g. Ludvigson et al. 1998; Driese et al. 2010; Robinson et al. 2010; Suarez et al. 2010). The range in $\delta^{13}C$ values of sphaerosiderite and spheroidal siderite, in general, and in this investigation, is large (–17.3 to –2.4‰ for sphaerosiderite and –10.1 to –5.1 ‰ for spheroidal siderite) (Table 1; Fig. 11). This may reflect either a variety in the microbes (bacteria and fermenters), which produced CO_2 / HCO_3^- for siderite precipitation, or it could represent a mixture of two different end-members of bicarbonate. Bicarbonate from the decomposition of organic matter in the suboxic zone represents the low $\delta^{13}C$ values of sphaerosiderite and spheroidal s, whereas bicarbonate originating from methanogenic fermentation of organic matter is responsible for the relatively high $\delta^{13}C$ values of the concretionary cement (Fig. 11; e.g. Irwin et al. 1977; Mozley and Wersin 1992; Ludvigson et al. 1998; Krajewski et al. 2010). The shift in $\delta^{13}C$ values (Fig. 11) is accompanied by a change in crystal morphology from radiating growth in sphaerosiderite to rhombohedral overgrowths and cement (Figs 7), which also may be explained by a shift from bacterially-mediated growth in the iron reduction zone to precipitation in the methanogenic zone.

The zonation within the perfectly zoned sphaerosiderites is caused by variation in carbonate mineralogy and chemistry, and reflects availability of Fe, Mn, Ca and Mg in the neighboring/local environment. The rate of iron reduction, and hence the availability of Fe^{2+}, is the limiting factor on precipitation of microbial siderite (Mortimer et al. 1997). In addition to Fe, Mn, Mg, Zn and Ca abundance in the fluids, variation in nutritional stress and physical conditions, for example temperature, also influence the iron reduction rate and hence the incorporation of other elements, like Mn (Mortimer et al. 1997). Coccoid morphology/clusters of sphaerosiderite and areas of sphaerosiderite with identical zonation pattern (Figs 7E and 8A) probably mark the outline of microbial communities. The zonation pattern within one microbial community may represent minor episodes of drying-out or harsh/hostile conditions for the microbes. During such dry periods, shrinkage, partial dissolution and alteration of the protruding outgrowths may ensure its spherical/rounded shape (Fig. 12).

Microscale variations reflecting groundwater fluctuations

Causes of zonation can be divided into two general explanations/hypotheses: 1) mixing of meteoric and marine waters (Mozley 1989; Choi et al. 2003) and 2) modification of the original pore waters during successive stages of microbial decomposition of organic matter (Mozley and Carothers 1992; Lim et al. 2004). The latter is almost identical to the explanation by Wilkinson et al. (2000) that siderite precipitation takes place during gradual burial within the Fe and Mn reduction zones, while dissolution takes place in the sulphate reduction zone, and siderite growth in the methanogenic zone.

The siderite morphologies found in the Boserup beds at Norra Albert provide two important contributions to this dispute on the origin of zonation due to their microscale and macroscale variations in morphology and stable isotope geochemistry. The observed microscale variations in siderite zonation pattern in the sphaerosiderites (Figs 7A, 7E, 8A, 8C) cannot be explained by either of the hypotheses described previously. Though marine excursions may have occurred in the Boserup beds during storm episodes, similar to the

marine occurrences in the Bjuv Member at other localities in Scania (Lindström and Erlström 2006), marine influxes in a meteoric-dominated environment ought to have affected all sphaerosiderites. The chemical composition is typically low in Mg and Ca for all siderite micromorphologies (Fig. 10), which suggests meteoric water composition (Matsumoto and Iijima 1981; Mozley 1989; Browne and Kingston 1993). Pyrite occurs rarely, and when present as a very early phase enclosed in the centre of the sphaerosiderite. This indicates that sulphate was limited from the time of deposition and that iron reduction took over instead of sulphate reduction. Furthermore, the $\delta^{18}O$ values in all siderite morphologies from Norra Albert are very consistent, close to the meteoric water composition, and show no influence from marine water (Fig. 11).

If the zonation pattern reflects depth-controlled burial processes (as suggested by Mozley and Carothers 1992; Wilkinson et al. 2000), then repeated small tectonic movements or variations in sedimentation rate/erosion would be required to explain the numerous changes through the Fe-reduction, Mn-reduction, sulphate reduction and methanogenic zones. These possibilities seem unlikely as the fluvial style of the Boserup beds does not change over this interval. Groundwater fluctuations seem a more likely explanation and are supported by additional features besides the perfectly zoned sphaerosiderite. Siderite cementation in shrinkage-fractures between detrital grains and sphaerosiderite could either be a result of mechanical compaction or caused by a period of shrinkage occurring during drying-out, either due to subaerial exposure or to lowering of the water table before siderite was again precipitated in the shrinkage fractures (Figs 7A, 12). The possibility that it could have been caused by mechanical compaction seems less likely, since fractured sphaerosiderites only occur in one concretion. Fluctuations in groundwater table would result in multiple changes in the physiochemical condition and the microbial life conditions. A longer growth period could explain the numerous zones and the necessity of using other metals, e.g. Mn and Zn, as the Fe source for the bacterial metabolism was exhausted. The presence of hematite suggests that siderite precipitation was followed by its alteration to iron-oxide/hydroxides in the unsaturated zone prior to burial diagenesis, as hematite replaced iron-oxide/hydroxides (not siderite) either due to aging (Van Houten 1961), which is less likely in Triassic – Jurassic sediments, or at enhanced temperatures (> 56°C) (Weibel 1999). The Triassic–Jurassic-boundary strata in Scania have been subjected to moderate burial temperatures < 85°C (inferred

from vitrinite reflectance by Ahlberg 1994) and > 65°C (due to restricted quartz diagenesis, in comparison with Weibel et al. 2010). Hence, fluctuations in groundwater level during deposition of the Boserup beds is the most plausible explanation for both sphaerosiderites with numerous zones of slightly varying composition, formation of hematite, and healing shrinkage cracks.

As elsewhere in NW Europe, the Danish part of the Norwegian–Danish Basin was subjected to major sea-level changes at this time, the "regression–transgression couplet" that may have been linked to tectonic movements during the formation of the Central Atlantic Magmatic Province (Hallam 1997; Hallam and Wignall 1999). The underlying Bjuv member is interpreted to have been deposited during a transgression and as part of a highstand systems tract (Petersen et al. 2013), with the maximum flooding surface MFS7 of Nielsen (2003) situated between coal seams B and A, whereas the Boserup beds, in contrast, were formed during a lowstand systems tract. However, these sea-level changes would not necessarily have caused repeated fluctuations in groundwater level during the deposition of the Boserup beds. The high proportion of structure less sandstones in the Boserup beds suggests rapid deposition, possibly from flash floods, rather than through bedform migration, and associated liquefaction/fluidization processes. A more extreme climate with increased humidity and storminess in the late Rhaetian (Petersen and Lindström 2012), strong seasonality with episodic storms of heavy rain, alternating with periods of enhanced drought, could be responsible for a fluctuating groundwater table. The co-occurrence of humid habitats and floral elements with xeromorphic features, i.e. features that may be linked to physiological drought, in the Rhaetian flora in Scania (Pott and McLoughlin 2011) may possibly also be ascribed to groundwater fluctuations or seasonal drought. There is also the possibility that the fluctuations in ground-water table were linked to increased repeated seismicity during this time (Lindström et al. 2015), because changes in groundwater levels are a common effect during earthquakes (Wang and Manga 2010). The perfectly zoned sphaerosiderites occur in the upper part of soft-sediment deformation structures – "seismites"– identified at both Norra Albert and in the Fleninge No. 266 core (Figs. 3A and C). Soft- sediment deformation structures form in unconsolidated, water-saturated sediments (e.g. Topal and Özkul 2014), and hence are likely to have formed close to the groundwater table. Fracturing and displacement of sphaerosiderite, followed by fracture healing (Fig. 7D),

show that local deformation occurred shortly after early diagenesis and could be related to mechanical compaction or soft-sediment deformation structures triggered by seismic events (Lindström et al. 2015).

Conclusions

The late Rhaetian terrestrial succession in northwestern Scania exhibits a variety of siderite micromorphologies, comprising perfectly zoned sphaerosiderite, poorly zoned sphaerosiderite (possibly identical with spherulitic siderite), spheroidal siderite and their rhombohedral and fibrous siderite overgrowths, enclosed in sparry, microspar and micritic concretionary siderite cement. The siderite formed in an apparently similar early diagenetic/pedogenic environment, as indicated by similar trace element variations and meteoric water oxygen isotopic compositions. The characteristic broad range in carbon isotopic compositions indicates that different microbes in the pedogenic environment were involved in degradation of organic matter and supplied C for siderite formation. Here the carbon isotopic composition can be subdivided into sphaerosiderite and spheroidal siderite of low values (–17.3 to –2.4‰ $\delta^{13}C$) and their rhombohedral or fibrous siderite overgrowths of almost similar values (–13.0 to +3.1‰ $\delta^{13}C$) sourced from bacterial degradation of organic matter in the Fe-reduction zone. This was followed by concretionary siderite cement of higher isotopic values (–5.8 to +7.8‰ $\delta^{13}C$) promoted by fermentation activity in the methanogenic zone. Growths of spheroidal siderite may have initiated on organic compounds, for example palynomorphs or stomata; likewise sphaerosiderite growth probably started on other, but specific, types of organic matter, which served as a microbial energy source and controlled the initial crystal growth.

Perfectly-zoned sphaerosiderite is restricted to the Boserup beds. The perfect multi-layered zonation is related to heterogeneous alteration caused by mineralogical and geochemical variations. The zonation reflects microbial activity, their life conditions, and availability of Fe, Mn, Ca and other cations in the pore water. These conditions are linked to amount of precipitation, water flow and groundwater-level fluctuations.

Intervals of continuous water-saturation and flow through the sediments resulted in Fe-rich siderite precipitation in the Fe-reduction zone. Under unsaturated or poorly saturated conditions, for example during episodes of lowered water table, rhodochrosite and Mn-rich siderite formed when the microbial community experienced hostile life conditions and/or the Fe supply was exhausted. The change from the saturated to unsaturated zone caused partial dissolution of poorly and perfectly zoned sphaerosiderite, which explains their continued spherical zonation and rounded shape. The inferred changes in groundwater level suggest deposition under a strongly seasonal climate with episodic drought. During burial the siderite precipitation style changed from bacterially mediated spherical and radiating growth in the Fe-reduction zone to rhombohedral precipitation in the methanogenic zone and still characterized by meteoric water of –5.1‰ $\delta^{18}O$ at a c. 45°N latitudinal position of Scania.

Acknowledgments

All concerned researchers benefitted from a grant from the Geocenter Denmark. Jette Halskov is thanked for drafting the figures. Thanks to Karsten Secher for providing a siderite standard from Ivigttuut, Greenland. This paper is published with permission from the Geological Survey of Denmark and Greenland. The Nordsim facility is operated as a joint Nordic consortium; this is Nordsim publication ###. Thanks are addressed to Professor Steven Driese and an anonymous reviewer for their thorough and constructive review which substantially improved the manuscript. Editor-in-Chief Brian Jones is thanked for his efficient handling of the manuscript.

References

Ahlberg, A. 1994. Deposition and diagenesis of the Rhaetian-Hettangian succession (Triassic-Jurassic) in southern Sweden: a synthesis. Lund Publication in Geology No. 123, 137p.

Ahlberg, A., Arndorff, L., Guy-Ohlson, D. 2002. Onshore climate change during the Late Triassic marine inundation of the Central European Basin. Terra Nova 14, 241–248.

Ahlberg, A., Olsson, I. and Šimkevičius, P. 2003.Triassic–Jurassic weathering and clay minerals dispersal in basement areas and sedimentary basins of southern Sweden. Sedimentary Geology 161, 15–29.

Anderson, T. F., Arthur, M. A. 1983. Stable isotopes of oxygen and carbon and their application to sedimentologic and palaeoenvironmental problems. In: Arthur, M. A., Anderson, T. F., Kaplan, I. R., Veizer, J., Land, L. S. (Eds.). Stable isotopes in sedimentary geology. SEPM course No. 10, Dallas 1983, 1-1–1-151.

Andrews, L. L. 2014.The Jurassic shales of the Weald Basin: geology and shale oil and shale gas resource estimation. Appendix G. British Geological Survey for Department of Energy and Climate Change, London, UK, 79p.

Baker, J. C., Kassan, J., Hamilton, P. J. 1996. Early diagenetic siderite as an indicator of depositional environment in the Triassic Rewan Group, southern Bowen Basin, eastern Australia. Sedimentology 43, 77–88.

Belcher, C.M., Mander, L., Rein, G., Jervis, F.X., Haworth, M., Hesselbo, S.P., Glasspool, I.J., McElwain, J.C. 2010. Increased fire activity at the Triassic/Jurassic boundary in Greenland due to climate-driven floral change. Nature Geoscience 3, 426–429.

Blachburn, T. J., Olsen, P. E., Bowring, S. A., McLean, N. M., Kent, D. V., Puffer, J., MacHone, G., Rasbury, E. T., Et-Touham, M. 2013. Zircon U-Pb geochronology links the end-Triassic extinction with the Central Atlantic Magmatic Province. Science 340, 941–945.

Blakey, R. 2016. Palaeomaps (http://cpgeosystems.com/paleomaps.html)

Bond, D. P. G. and Wignall, P. B. 2014. Large igneous provinces and mass extinctions: An update. Geological Society of America Special Publication 505, 29–56.

Bojanowski, M. J., Jaroszewicz, E., Košir, A., Łoziński, M., Marynowski, L., Wysocka, A., Derkowski, A. 2016. Root-related rhodochrosite and concretionary siderite formation in oxygen-deficient conditions induced by a ground-water table rise. Sedimentology 63, 523 – 551.

Browne, G. H, Kingston, D. M. 1993. Early diagenetic spherulitic siderites from Pennsylvanian palaeosols in the Boss Point Formation, Maritime Canada. Sedimentology 40, 467–474.

Carothers, W. W., Adami, L. H., Rosenbauer, R. J. 1988. Experimental oxygen isotope fractionation between siderite-water and phosphoric acid liberated CO_2-siderite. Geochimica et Cosmochimica Acta 52, 2445– 450.

Choi, K. S., Khim, B. K. & Woo, K. S. 2003. Spherulitic siderites in the Holocene coastal deposits of Korea (eastern Yellow Sea). Elemental and isotopic composition and depositional environment. Marine Geology 202, 17–31.

Cleveland, D.M., Nordt, L.C., Dworkin, S.I., Atchley, S.C. 2008. Pedogenic carbonate isotopes as evidence for extreme climatic events preceding the Triassic–Jurassic boundary: Implications for the biotic crisis. Geological Society of America Bulletin 120, 1408–1415.

Craig, H. 1957. Isotopic standards for carbon and oxygen correction factors for mass spectrometric analysis of carbon dioxide. Geochimica et Cosmochimica Acta 12, 133–149.

Driese, S. G., Ludvigson, G. A., Roberts, J. A., Fowle, D. A., González, Smith, J. J., Vulava, V. M., McKay, L. D. 2010. Micromorphology and stable-isotope geochemistry of historical pedogenic siderite formed in PAH contaminated alluvial clay soils, Tennessee, U.S.A. Journal of Sedimentary Research 80, 943–954.

Friedman, I., O'Neil, J. R. 1977. Compilation of stable isotopic fractionation factors of geochemical interest. US Geological Survey Prof. Paper 440-KK, 12 pp.

Fischer, M. J., Mudge, D. C. 1998. Triassic. In: Glennie, K. W. (Ed.) Petroleum geology in the North Sea – Basic concepts and recent advances 4th edition. Blackwell Sciences, 212–244.

Fisher, Q. J., Raiswell, R., Marshall. J. D. 1998. Siderite concretions from nonmarine shales (Westphalian A) of the Pennines England: Controls on their growth and composition. Journal of Sedimentary Research 68, 1034–1045.

Fritz, P., Binda, P. L., Folinsbee, F. E., Krouse, H. R. 1971. Isotopic composition of diagenetic siderites from Cretaceous sediments in Western Canada. Journal of Sedimentary Petrology 41, 282–288.

Gránásy, L., Pusztai, T., Tegze, G., Warren, J. A., Douglas, J. F. 2005. Growth and form of spherulites. Physical Review E 72, 011605-1 – 011605-15.

Hallam, A. 1997. Estimates of the amount and rate of sea-level change across the Rhaetian–Hettangian and Pliensbachian–Toarcian boundaries (latest Triassic to early Jurassic). J. Geol. Soc. London 154, 773–779.

Hallam, A., Wignall, P.B. 1999. Mass extinctions and sea-level changes. Earth-Science Reviews 48, 217–250.

Hesselbo, S. P., Robinson, S. A., Surlyk, F., Piasecki, S. 2002. Terrestrial and marine extinction at the Triassic-Jurassic boundary synchronized with a major carbon-cycle perturbation: A link to initiation of massive volcanism? Geology 30, 251–254.

Irwin, H., Curtis, C. D., Coleman, M., 1977. Isotopic evidence for source of diagenetic carbonates formed during burial of organic-rich sediments. Nature 269, 209–213.

Krajewski, K. P., Gonzhurov, N. A., Laiba, A.A., Tatur, A. 2010. Early diagenetic siderite in the Panorama Point Beds (Radok Conglomerate, Early to Middle Permeian), Prince Charles Mountains, East Antarctica. Polish Polar Research 31, 169–194.

Köhler, I., Konhauser, K. O, Papineau, D., Bekker, A., Kappler, A. 2013. Biological carbon precusor to diagenetic siderite with spherical structrues in iron formations. Nature Communication 4:1741 DOI: 10.1038/ncomms 2770.

Liboriussen, J., Ashton, P., Thygesen, T. 1987. The tectonic evolution of the Fennoscandian Border Zone in Denmark. In: Ziegler, P. A. (ed.), Compressional intra-plate deformations in the Alpine Foreland. Tectonophysics 137, 21–29.

Lim, D. I., Jung, H. S, Yang, S. Y., Yoo, H. S. 2004. Sequential growth of early diagenetic freshwater siderites in the Holocene coastal deposits, Korea. Sedimentary Geology 169, 107–120.

Lindström S., Erlström, M. 2006. The late Rhaetian transgression in southern Sweden: Regional (and global) recognition and relation to the Triassic – Jurassic boundary. Palaeogeography, Palaeoclimatology, Palaeoecology 241, 339–372.

Lindström, S., van de Schootbrugge, B., Dybkjær, K., Pedersen, G. K., Fiebig, J., Nielsen, L. H., Richoz, S. 2012. No causal link between terrestrial ecosystem change and methane release during the end-Triassic mass extinction. Geology 40, 531–534.

Lindström, S., Pedersen, G. K., van de Schootbrugge, B., Hansen, K. H., Kuhlmann, N., Thein, J.,Johansson, L., Petersen, H. I., Alwmark, C., Dybkjær, K., Weibel, R., Erlström, M., Nielsen, L. H.. Oschmann, W., Tegner, C. 2015. Intense and widespread seismicity during the end-Triassic mass extinction due to emplacement of a large igneous province. Geology 43, 387–390.

Lund, J. J. 1977. Rhaetic to Lower Liassic palynology of the onshore south-eastern North Sea Basin. Geological Survey of Denmark II Series, 109, 105p.

Ludvigson, G. A., González, L. A., Mtzger, R. A., Witzke, B. J., Brenner, R. L., Murillo, A. P., White, T. S. 1998. Meteoric sphaerosiderite lines and their use for paleohydrology and paleoclimatology. Geology 26, 1039–1042.

Marynowski, L., Simonet, B.R.T., 2009. Widespread Upper Triassic to Lower Jurassic wildfire records from Poland: Evidence from charcoal and pyrolytic polycyclic aromatic hydrocarbons. Palaios 24, 785–798.

Matsumoto, R., Iijima, A. 1981. Origin and diagenetic evolutionof Ca-Mg-Fe carbonates in some coalfields of Japan. Sedimentology 28, 239–259.

McElwain, J.C., Beerling, D.J., Woodward, F.I. 1999. Fossil plants and global warming at the Triassic – Jurassic boundary. Science 285, 1386–1390.

Metcalfe, I. 2011. Tectonic framework and Phanerozoic evolution of Sundaland. Gondwana Research 19, 3–12.

Mogensen, T. E., Kortsgård, J. A. 2003. Triassic and Jurassic transtension along part of the Sorgenfrei–Tornquist Zone in the Danish Kattegat. In: Ineson, J. R., Surlyk, F. (Eds.), The Jurassic of Denmark and Greenland. Geological Survey of Denmark and Greenland Bulletin 1, 439–458.

Mortimer, R. J. G., Coleman, M. L., Rae, J. E. 1997. Effect of bacteria on the elemental composition of early diagenetic siderite: implications for palaeoenvironmental interpretations. Sedimentology 44, 759–765.

Mozley, P.1989. Relation between depositional environment and the elemental composition of early diagenetic siderite. Geology 17, 704–706.

Mozley, P. S., Carothers, W. W. 1992. Elemental and isotopic composition of siderite in the Kuparuk Formation, Alaska: Effect of microbial activity and water/sediment interaction on early pore-water chemistry. Journal of Sedimentary Petrology 62, 681–692.

Mozley, P. S., Wersin, P. 1992.Isotopic composition of siderite as an indicator of depositional environment. Geology 20, 817–820.

Nielsen, L. H. 2003. Late Triassic-Jurassic development of the Danish Basin and the Fennoscandian Border Zone, southern Scandinavia. In: Ineson, J. R., Surlyk, F. (Eds.), The Jurassic of Denmark and Greenland. Geological Survey of Denmark and Greenland Bulletin, 459–526.

Petersen, H. I., Lindström, S. 2012. Synchronous wildfire activity rise and mire deforestation at the Triassic-Jurassic boundary. PLoS One 7(10) e47236.doi:10.1371, 15pp.

Petersen, H. I., Lindström, S., Therkelsen, J., Pedersen, G. K. 2013. Deposition, floral composition and sequence stratigraphy of uppermost Triassic /Rhaetian) coastal coals, southern Sweden. International Journal of Coal Geology 116-117, 117–134.

Pott, C., McLoughlin, S. 2011. The Rhaetian flora of Rögla, northern Scania, Sweden. Palaeontology 54, 1025–1051

Retallack, G.J. 1997. Paleosols in the Upper Narrabeen group of New South Wales as evidence of Early Triassic palaeoenvironments without exact modern analogues. Australian Journal of Earth Sciences 44, 185–201.

Robinson, S. A., Scotchman, J. I., White, T. S., Atkinson, T. C. 2010. Constraints on palaeoenvironments in the Lower Cretaceous Wealden of southern England, from the geochemistry of sphaerosiderites. Journal of the Geological Society, London, 167, 303–311.

Rosenbaum, J. M., Sheppard, S. M. F. 1986. An isotopic study of siderites, dolomites and ankerites at high temperatures. Geochimica et Cosmochimica Acta 50, 1147–1150.

Rosenau, N. A., Tabor, N. J., Elrick, S. D., Nelson, J. W. 2013. Polygenetic history of paleosols in Middle – Upper Pennsylvanian cyclothems of the Illinois Basin, U.S.A.: Part I. Characterization of paleosol types and interpretation of pedogenic processes. Journal of Sedimentary Research 83, 606–636.

Ruhl, M., Bonis, N. R., Reichart, G.-J., Damsté, J. S., Kürschner, W. M. 2011. Atmospheric carbon injection linked to end-Triassic mass extinction. Science 233, 430–434.

Schoene, B., Guex, J., Batrtolini, A., Schaltegger, U., Blackburn, T. J. 2010. Correlating the end-Triassic mass extinction and flood basalt volcanism at the 100 ka level. Geology 38, 387–390.

Sholkovitz, E. R., Copland, D. 1981. The coagulation, solubility and adsorption properties of Fe, Mn, Cu, Ni, Cd, Co and humic acid in river water. Geochimica et Cosmochimica Acta 45, 181–189.

Sivhed, U. 1984: Litho- and biostratigraphy of the Upper Triassic-Middle Jurassic in Scania, southern Sweden. Sveriges geologiska Undersökning, Ser. C, No. 806, 31 pp.

Steinthorsdottir, M., Woodward, F. I., Surlyk, F., McElwain, J. C. 2012. Deep-time evidence of a link between elevated CO_2 concentrations and perturbations in the hydrological cycle via drop in plant transpiration. Geology 40, 815–818. Suarez, M. B., González, L. A., Ludvigson, G. A. 2010. Estimating the oxygen isotopic composition of equatorial precipitation during the Mid-Cretaceous. Journal of Sedimentary Research 80, 480–491.

Topal, S., Özkul, M. 2014. Soft-sediment deformation structures interpreted as seismites in the Kolankaya Formation, Denizli Basin (SW Turkey). The Scientific World Journal 2014, dx.doi.org/10.1155/2014/352654, 13pp.

Troedsson, G. 1951. On the Höganäs series of Sweden (Rhaeto-Lias). Lunds Universitets Årsskrift, N. F. 47, 269p.

Ufnar, D. F., Gonzáles, L. A., Ludvigson, A., Brenner, R. L., Witzke, B. J. 2001. Stratigraphic implications of meteoric sphaerosiderite $\delta^{18}O$ values in paleosols of the Cretaceous (Albian) Boulder Creek Formation, NE British Columbia Foothills, Canada. Journal of Sedimentary Research 71, 1017–1028.

Ufnar D. F., Gonzáles, L.A., Ludvigson, G.A., Brenner, R.L., Witzke, B.J. 2002. The mid-Cretaceous water bearer: isotope mass balance quantification of the Albian hydrologic cycle. Palaeogeography, Palaeoclimatology, Palaeoecology 188, 51–71.

Ufnar, D.F., Ludvigson, G.A., Gonzáles, L.A.,Brenner, R.L., Witzke, B.J. 2004a. High latitude meteoric $\delta^{18}O$ compositions: paleosol siderite in the mid-Cretaceous Nanushuk Formation, North Slope Alaska. Geological Society of America Bulletin 116, 63–159.

Ufnar, D. F., González, L. A., Ludvigson, G. A., Brenner, R. L., Witzkes, B. J. 2004b. Diagentic overprinting of the sphaerosiderite palaeoclimate proxy: are records of pedogenic groundwater $\delta^{18}O$ values preserved? Sedimentology 51, 127–144.

van de Schootbrugge, B., Quan, T. M., Lindström, S., Püttmann, W., Heunisch, C., Pross, J., Fiebig, J., Petschick, R., Röhling, H.-G., Richoz, S., Rosenthal, Y., Falkowski, P. G. 2009. Floral changes across the Triassic/Jurassic boundary linked to flood basalt volcanism. Nature Geoscience 2, 589–594.

Van Houten, F. B. 1961. Climatic significance of red beds. In: Nairn, A. E. M (Ed.) Descriptive palaeoclimatology. Interscience Publishers Inc, New York, 89–139.

Wang, C.-Y., Manga, M. 2010. Hydrologic responses to earthquakes and a general metric. Geofluids 10, 206–216.

Weibel, R. 1999. Effects of burial on the clay assemblage in the Triassic Skagerrak Formation. Clay Minerals 34, 619–635.

Weibel, R., Friis, H., Kazerouni, A. M., Svendsen, J. B., Stokkendahl, J., Poulsen, M. L. 2010. Development of early diagenetic silica and quartz morphologies – Examples from the Siri Canyon, Danish North Sea. Sedimentary Geology 228, 151–170.

Wilkinson, M., Haszeldine, R. S., Fallick, A. E., Osborne, M. J. 2000. Siderite zonation within the Brent Group: microbial influence or aquifer flow? Clay Minerals 35, 107–117.

Figure captions

Table 1.

Sphaerosiderite occurrences, their geological background, morphology and geochemistry.

Fig. 1.

Stratigraphy of southern Sweden, which is compared with changes in sphaerosiderite occurrence (Troedsson 1951 and this study), dominating clay mineralogy (Ahlberg et al. 2003), occurrence of coal and remnants after wildfire activity (Troedsson 1951; Petersen and Lindström 2012) and palynozones (Lund 1977 and this study). Transgressive events are indicated (arrows), including MFS7, which is an important surface for correlation in the region (Nielsen 2003).

Fig. 2.

Map showing location of the Norra Albert quarry and the wells Albert-1 and Fleninge No. 266. Note that the position of the Norra Albert quarry and the Albert-1 well are identical.

Fig. 3.

Sedimentary logs showing typical siderite morphologies for the investigated samples.

A. Sedimentary log of the northern wall in the Norra Albert quarry.
B. Sedimentary log of the Albert-1 core.
C. Constructed sedimentary log of the Fleninge No. 266 well based on the description by Troedsson (1951).

Dimensions given in the diagrams are those of sphaerosiderite, spheroidal and rhombohedral siderite, not the dimensions of the concretions.

Fig. 4. Fieldwork Norra Albert quarry.

A. Overview of the northern wall in Norra Albert quarry. The 'Boserup beds' are the whitish grey deposits with local siderite concretions; the dark grey deposits of the Bjuv Member are partly covered by scree. The line marks the boundary between the 'Boserup beds' and the Bjuv Member. Arrows indicate some of the largest concretions.

B. Petrified wood enclosed in a siderite concretion.

C. Undulating siderite concretion following the sedimentary structures.

D. Close up of A.

E. Thick siderite concretion with a middle plane following the sedimentary structures, similar to the concretionary development in C, and surrounded by growth that cuts the sedimentary structures. Thegrowth probably started along the most coarse-grained sands and continued both upwards and downwards into the more fine-grained sandstones.

F. Close up of white box in E. The sedimentary structures seem to end at the concretionary interface, but thin section investigations have shown that sedimentary structures actually continue through the cemented area.

Fig. 5. An early displacive growth of siderite is documented by the high siderite content in concretions compared with sandstones in the Norra Albert quarry. The mineral content is calculated from chemical composition of bulk rock samples.

Fig. 6. Poorly zoned sphaerosiderites (spherulites, spherulitic siderite)

A. Poorly zoned sphaerosiderite (Si) with a low content of Ca and/or Mn commonly having central dissolution voids (marked by black arrows). Norra Albert quarry, 516816. Back –scatter electron (BSE) image.

B. Poorly zoned sphaerosiderite (Si) with incipient dissolution in the centre and rims of dissolution void around the central spherical part. The most intensive dissolution accompanies the centre having a small Ca content (compare EDS analyses 1 and 2). Norra Albert quarry, 516807. BSE image.

C. Poorly zoned sphaerosiderite (Si) with central dissolution void containing possible authigenic quartz (Q) and un-compacted kaolinite (Ka) and surrounded by compacted kaolinite. Fleninge No. 266, 151.62 m. BSE image.

D. Poorly zoned sphaerosiderite (Si) (EDS analysis 3) with a centre possibly made up of iron-oxide/hydroxide (Fe-ox) having a low content of Mn (EDS analysis 4). Norra Albert quarry, 516824. BSE image.

Fig. 7. Perfectly zoned sphaerosiderites

A. Zoned sphaerosiderites replaced by iron-oxides/hydroxides (Fe). Note that the sphaerosiderite at some point has lost contact to their growth substratum, however this has healed later. Norra Albert quarry, 516818. Reflected light image.

B. Broken perfectly zoned sphaerosiderite with healing rhombohedral siderite that appears the same as the overgrowth on the sphaerosiderite. Later exposure to oxidising water has resulted in replacement by iron-oxides/hydroxides (Fe). Norra Albert quarry, 516818. BSE image.

C. Microcrystalline anhedral siderite (Si) tightly fills the pore space between the sphaerosiderite and detrital grains. The detrital grains (Q) are dispersed and do not exhibit intergranular contacts, which indicate displacive and/or replacive growth of siderite. Alteration and replacement by iron-oxides/hydroxides (Fe) is probably related to oxidation of siderite along fracture wall probably due to percolation of oxygenated fluids. Norra Albert quarry, 516824D. BSE image.

D. Zoned sphaerosiderites replaced by iron-oxides/hydroxides (Fe). Altering zones seem to be almost similar for a specific area/concretion. The apparent variation in zonation pattern may be caused by different intersection planes. Norra Albert quarry, 516818. BSE image.

E. Fine-crystalline morphology of the inner part of the sphaerosiderite, which is ripped out, and coarser crystals as an outer rim. Norra Albert quarry, 516818. Secondary electron (SE) image.

F. Rhombohedral habit of siderite crystals forming an overgrowth on the sphaerosiderite. Norra Albert quarry, 516818. SE image.

Fig. 8. Varieties of zoned sphaerosiderites

A. Sphaerosiderite with relatively high content of Mn in the inner core (EDS analysis 1), followed by a rhodochrosite rim (EDS analysis 2) with dissolution voids (white arrows) and an outermost rim of low-Mn siderite . Norra Albert quarry, 516819. BSE image.
B. Cluster of rhodochrosite rimed sphaerosiderite enclosed in sparry siderite cement. Norra Albert quarry, 516819. SE image.
C. Concentric and sector zoned sphaerosiderite having a low content of Ca (EDS analysis 3), whereas the alteration rims show siderite with low contents of Si and possible Zn (EDS analysis 4). Norra Albert quarry, 516820. BSE image.
D. Round siderite core covered by rhombohedral siderite, which is partly dissolved and altered to iron-oxides/hydroxides. Norra Albert quarry, 516825. SE image.

Fig. 9. Spheroidal siderite (pseudomorphs after stomata)

A. Spheroidal siderite with radiating growth around a spheroidal core and in zones. Norra Albert quarry, 516824C. Transmitted light image, crossed nicols.
B. Spheroidal siderite with marked spheroidal zones. Norra Albert quarry, 516824C. Reflected light image.
C. Spheroidal siderite with radiating growth in spheroidal zones. Acid treated sample, Norra Albert quarry, 516824C. SE image.

Fig. 10 Chemical composition

Microprobe analyses show that siderite generally has a low content of Mg and Ca, though commonly relatively high content of Mn. The highest Mn contents typically occur in spheroidal siderite, perfectly zoned sphaerosiderite and their overgrowths, whereas the highest Ca contents occur in poorly zoned sphaerosiderite.

Fig. 11. Isotopic composition

A. IRMS (isotope ratio mass spectrometry) shows a narrow $\delta^{18}O$ composition and a large span in $\delta^{13}C$ values for bulk rock samples. Also perfectly zoned sphaerosiderite with zones of rhodochrocite groups together with other siderite samples.

B. SIMS (secondary ion mass spectrometry) of specific siderite morphologies in thin sections shows that perfectly zoned sphaerosiderite, spheroidal siderite and their siderite overgrowths have similar and lower $\delta^{13}C$ values than the siderite concretionary cement.

SIMS and IRMS analyses show similar $\delta^{18}O$ values for all siderite micromorphologies and the concretionary cement, which reflect end-Triassic groundwater composition. This fits with the likely meteoric water composition (indicated by the vertical blue lines) according to the Triassic – Jurassic middle latitude position at 45°N of Sweden (Anderson and Arthur 1983; Metcalfe 2011; Blakey 2016).

Fig. 12. Overview of siderite precipitation

Diagram showing an overview of the precipitation and growth of the different siderite morphologies in relation to other diagenetic features.

Figure captions

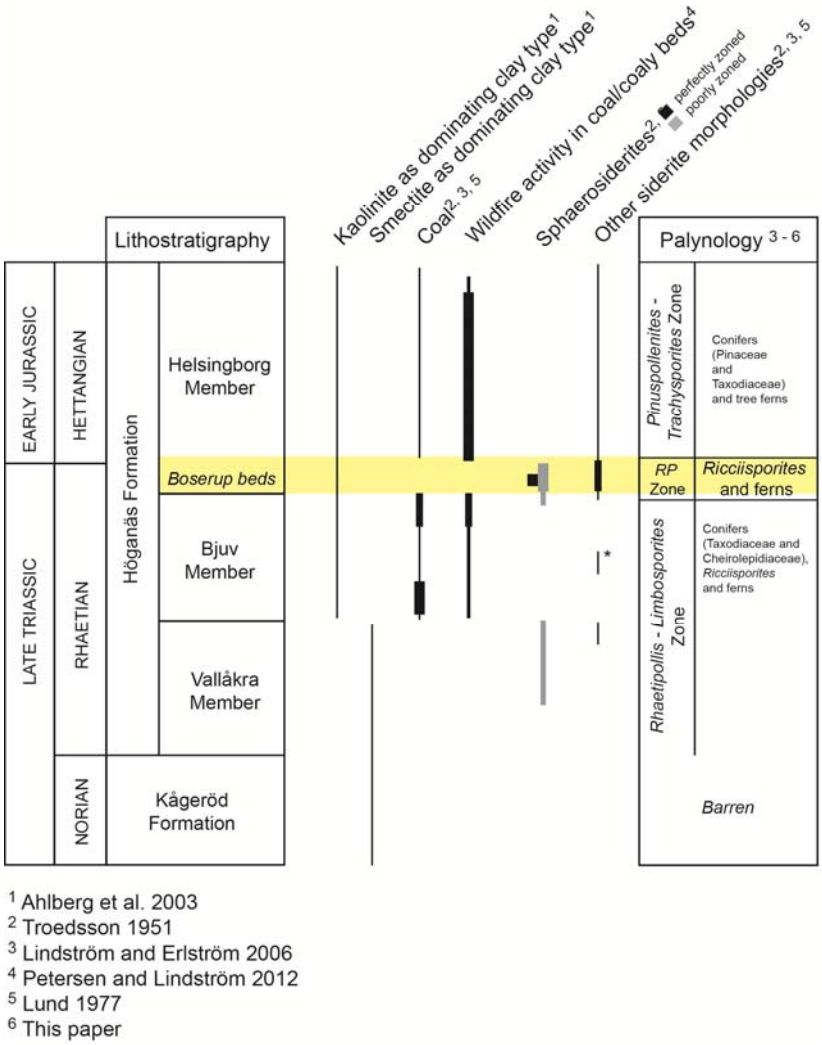

Fig. 1.

Stratigraphy of southern Sweden based on changes in sphaerosiderite occurrence (Troedsson 1951 and this study), dominating clay mineralogy (Ahlberg et al. 2003), occurrence of coal and remnants after wildfire activity (Troedsson 1951; Petersen and Lindström 2012) and palynozoes (Lund 1977 and this study). Transgressive events are indicated (arrows), including MFS7, which is an important surface for correlation in the region (Nielsen 2003).

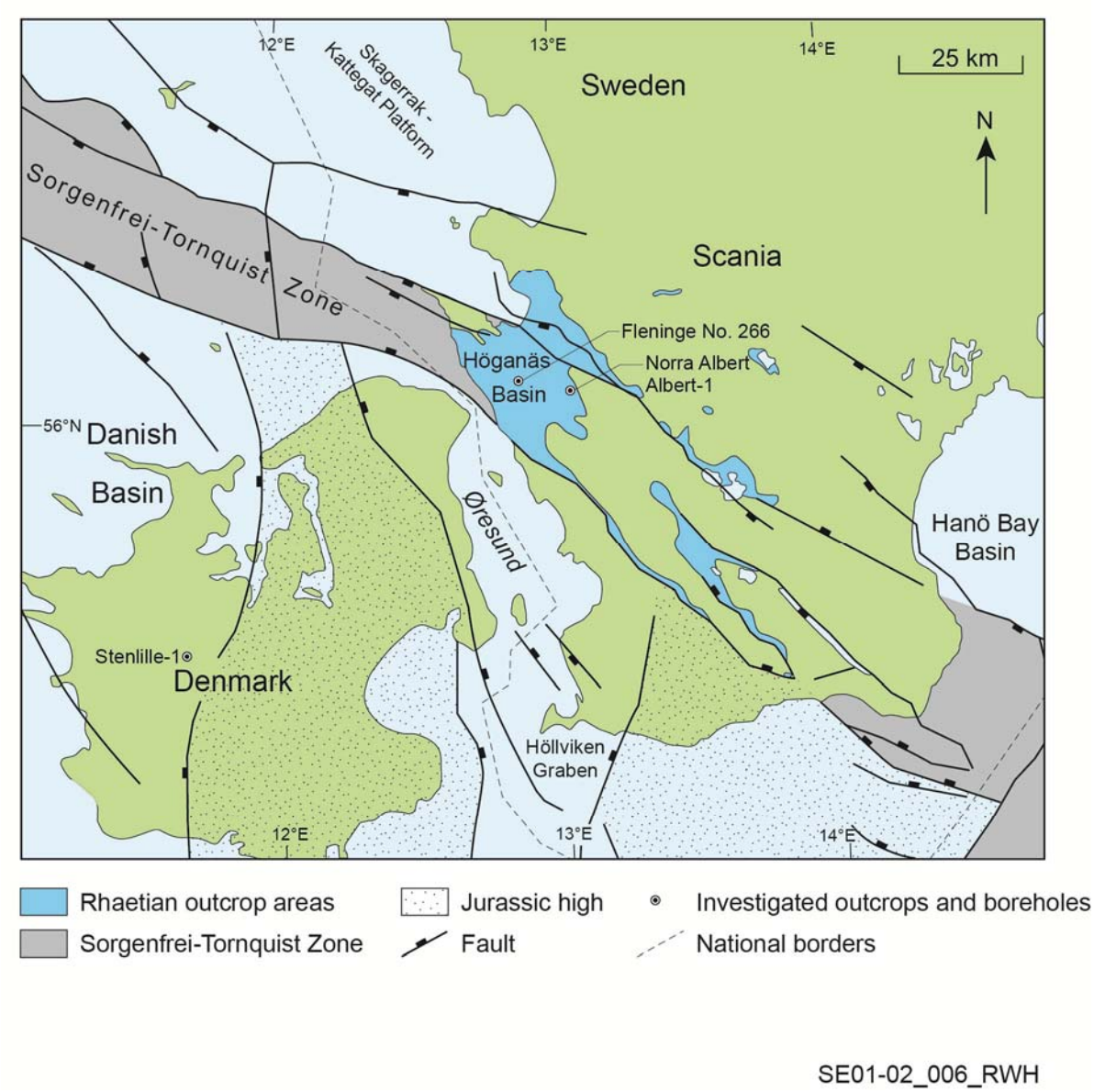

Fig. 2.

Map showing location of the Norra Albert quarry and the wells Albert-1 and Fleninge No. 266. Note that the position of the Norra Albert quarry and the Albert-1 well are identical.

Perfectly zoned sphaerosiderite

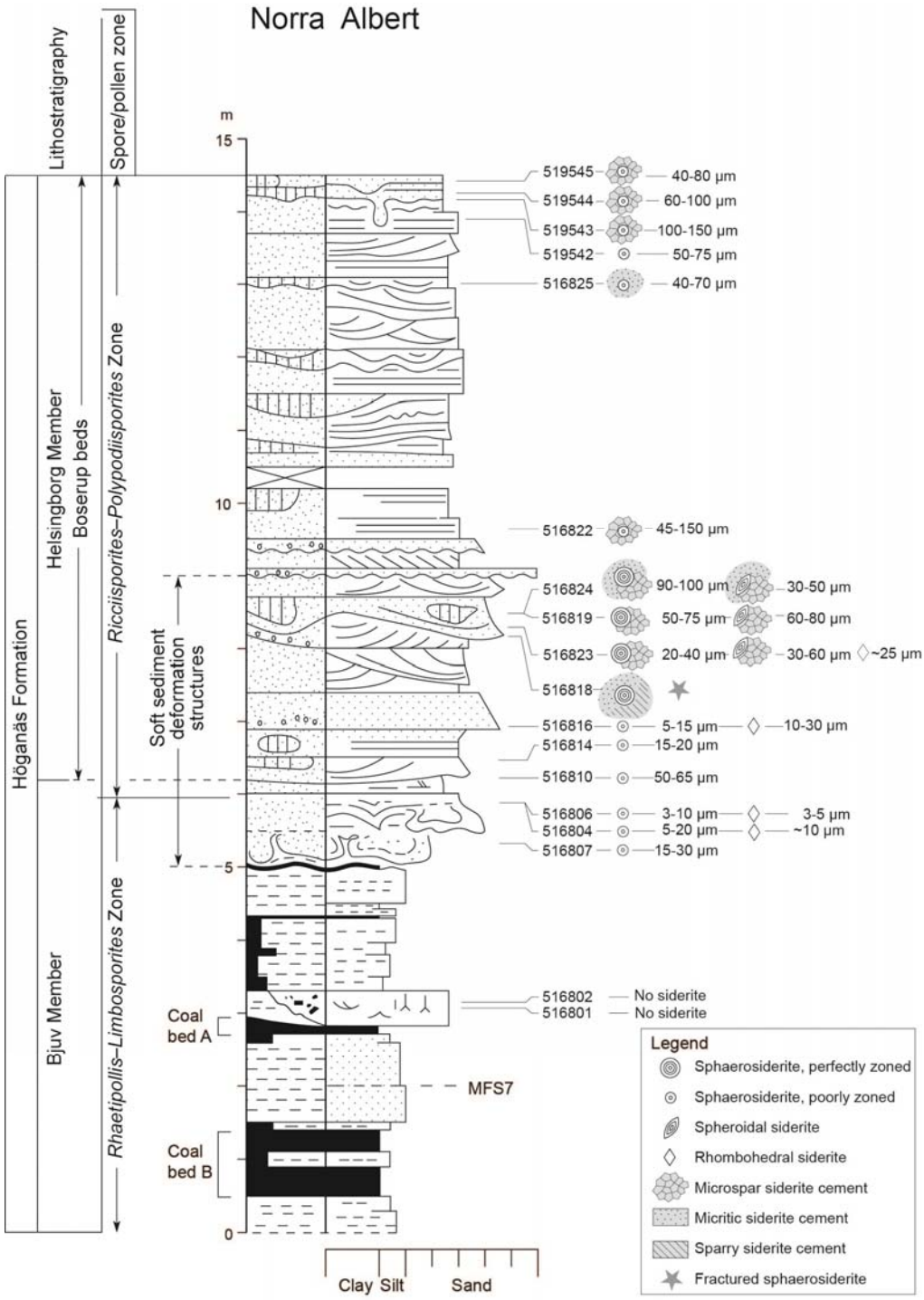

Perfectly zoned sphaerosiderite

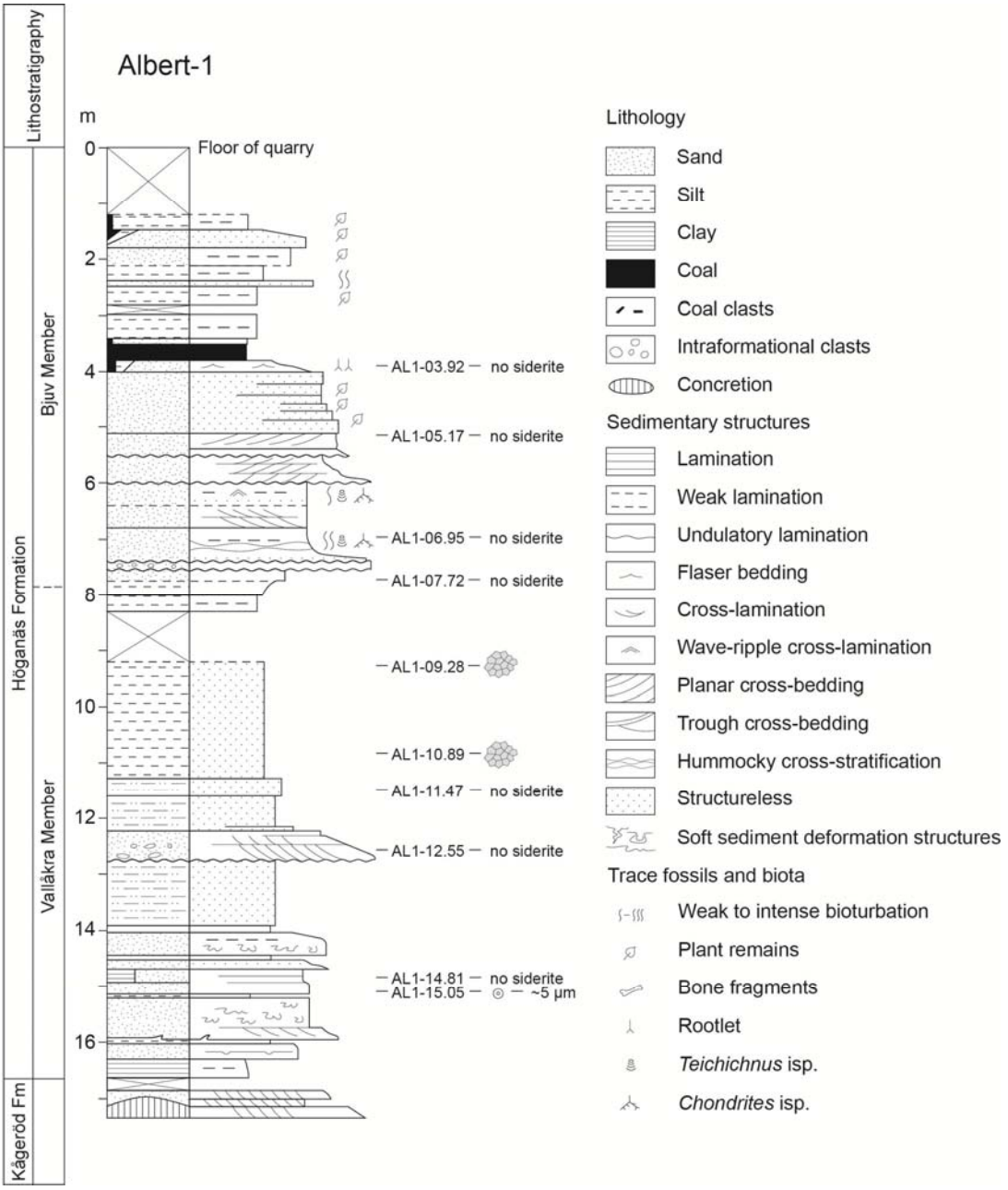

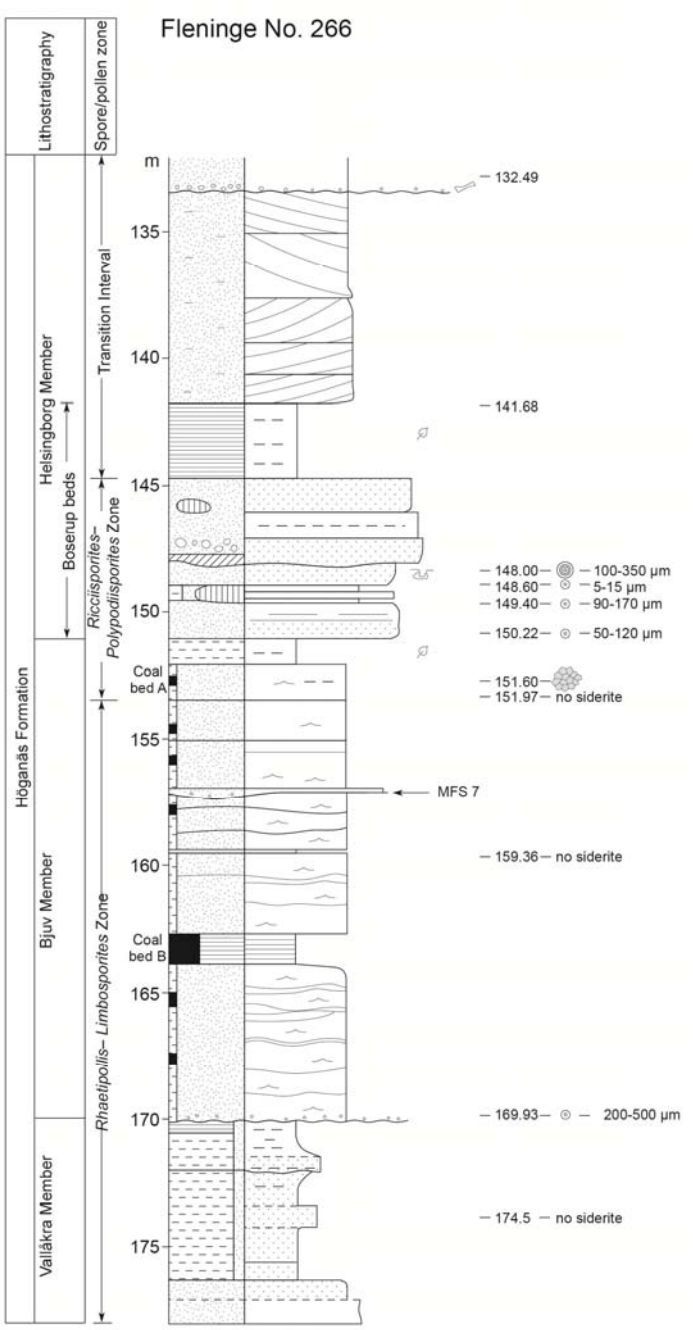

Fig. 3.

Sedimentary logs showing typical siderite morphologies for the investigated samples.

A. Sedimentary log of the northern wall in the Norra Albert quarry.
B. Sedimentary log of the Albert-1 core.
C. Constructed sedimentary log of the Fleninge No. 266 well based on the description by Troedsson (1951).

Dimensions given in the diagrams are those of sphaerosiderite, spheroidal and rhombohedral siderite, not the dimensions of the concretions.

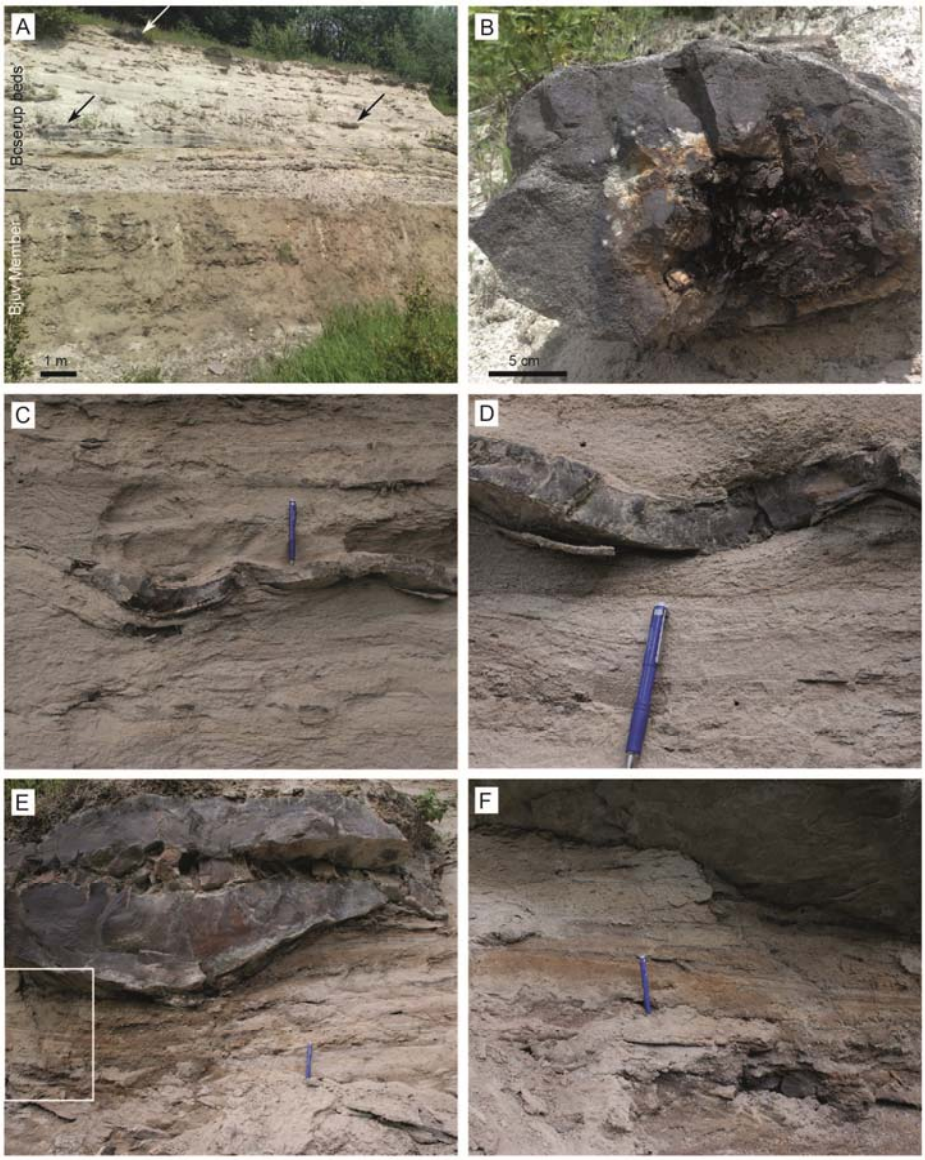

Fig. 4. Fieldwork Norra Albert quarry.

A. Overview of the northern wall in Norra Albert quarry. The 'Boserup beds' are the whitish grey deposits with local siderite concretions; the dark grey deposits of the Bjuv Member are partly covered by scree. The line marks the boundary between the 'Boserup beds' and the Bjuv Member.
B. Petrified wood enclosed in a siderite concretion.
C. Undulating siderite concretion following the sedimentary structures.
D. Close up of A.
E. Thick siderite concretion, which probably started along the most coarse-grained sands, similar to the morphology in C, and continued both upwards and downwards.
F. Close up of white box in E. The sedimentary structures seem to end at the concretionary interface, but thin section investigations have shown that sedimentary structures actually continue through the cemented area.

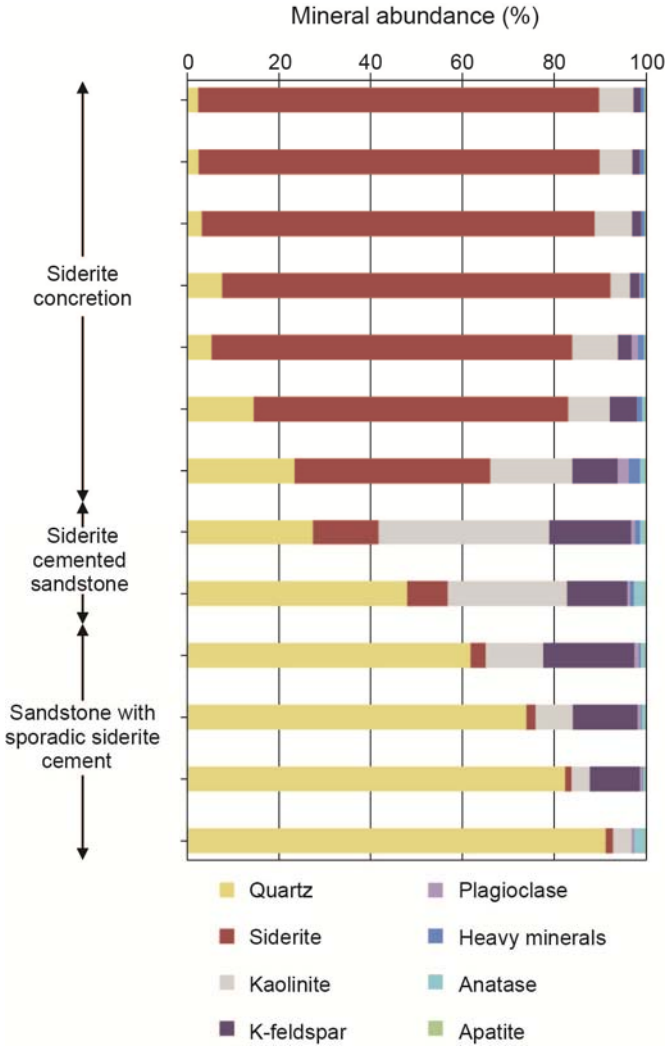

Fig. 5. An early displacive growth of siderite is documented by the high siderite content in concretions compared with sandstones in the Norra Albert quarry. The mineral content is calculated from chemical composition of bulk rock samples.

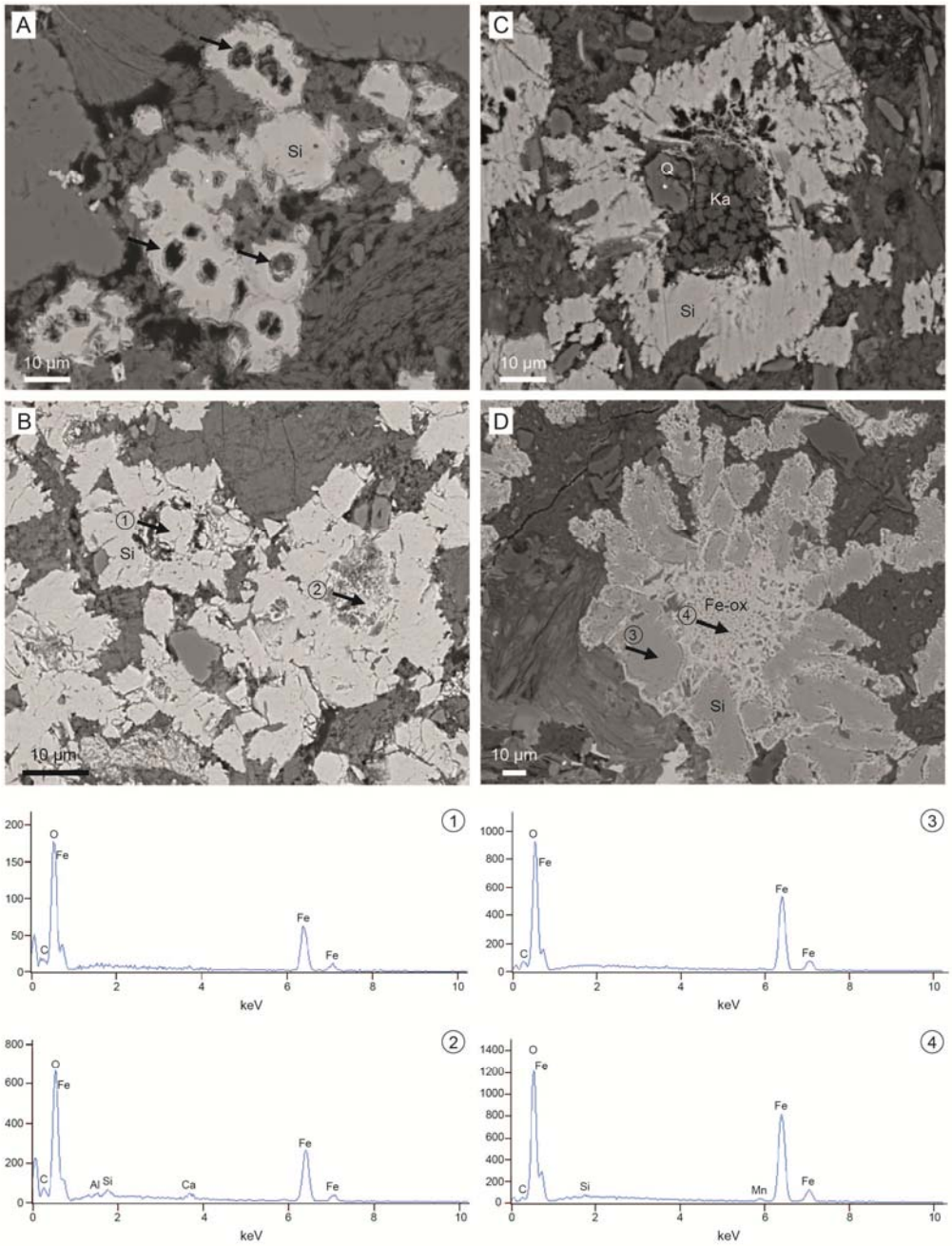

Fig. 6. Poorly zooned sphaerosiderites (spherulites, spherulitic siderite)

A. Poorly zoned sphaerosiderite. Norra Albert quarry, 516816. Back -scatteredelectron (BSE) image.

B. Poorly zoned sphaerosiderite with incipient dissolution in the centre and rims of dissolution void around the central spherical part. Norra Albert quarry, 516807. BSE image.

C. Poorly zoned sphaerosiderite with central dissolution void containing authigenic quartz (Q) and un-compacted kaolinite (Ka) and surrounded by compacted kaolinite. Fleninge No. 266, 151.62 m. BSE image.

D. Poorly zoned sphaerosiderite with a centre possibly made up of iron-oxide/hydroxide. Norra Albert quarry, 516824. BSE image.

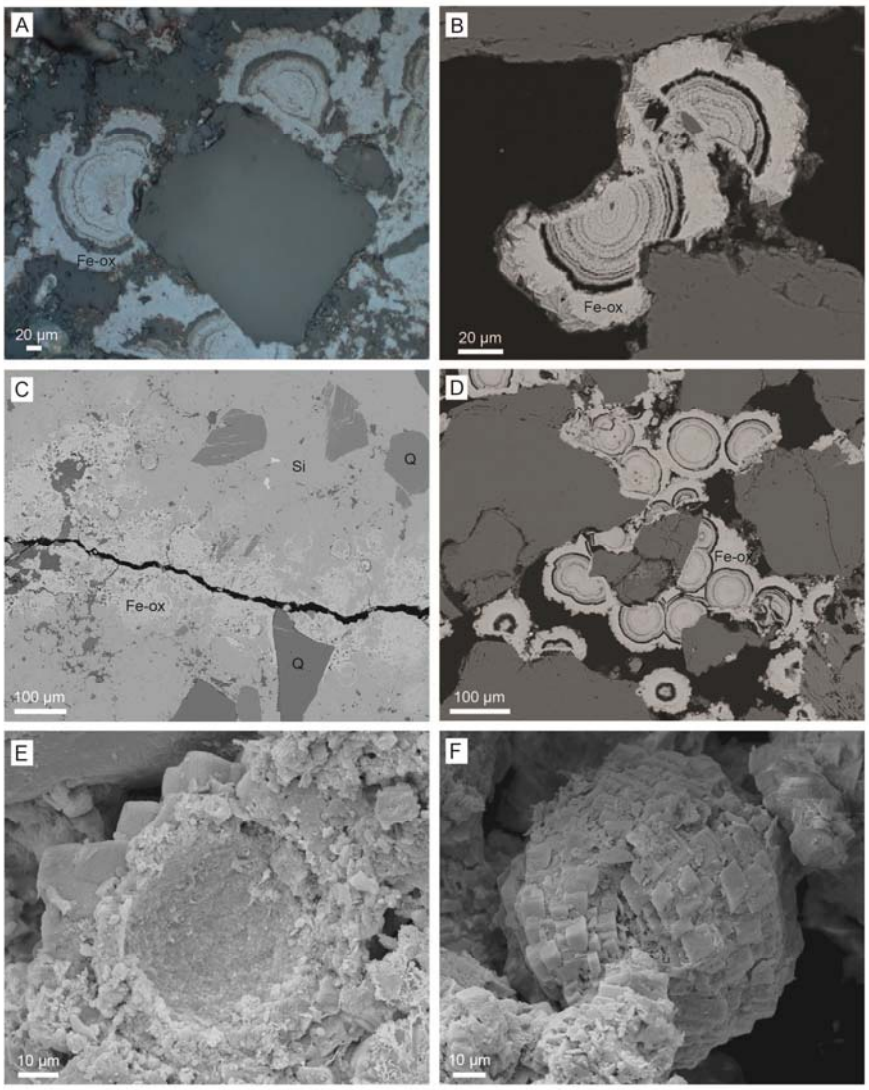

Fig. 7. Perfectly zoned sphaerosiderites

A. Zoned sphaerosiderites. Note that the sphaerosiderite at some point has lost contact to their growth substratum, however this has healed later. Norra Albert quarry, 516818. Reflected light image
B. Apparently poikilotopic siderite cement, which reveals the presence of sphaerosiderite along a fracture where alteration has penetrated. Norra Albert quarry, 516824D. BSE image.
C. Fine-crystalline morphology of the inner part of the sphaerosiderite, which is ripped out, and coarser crystals as an outer rim. Norra Albert quarry, 516818. Secondary electron (SE) image.
D. Broken perfectly zoned sphaerosiderite, which later has healed. Norra Albert quarry, 516818. BSE image.
E. Zoned sphaerosiderites. Altering zones seem to be similar for a specific area, here two different types of zonation is shown. Norra Albert quarry, 516818. BSE image.
F. Siderite crystals covering the sphaerosiderite. Norra Albert quarry, 516818. SE image.

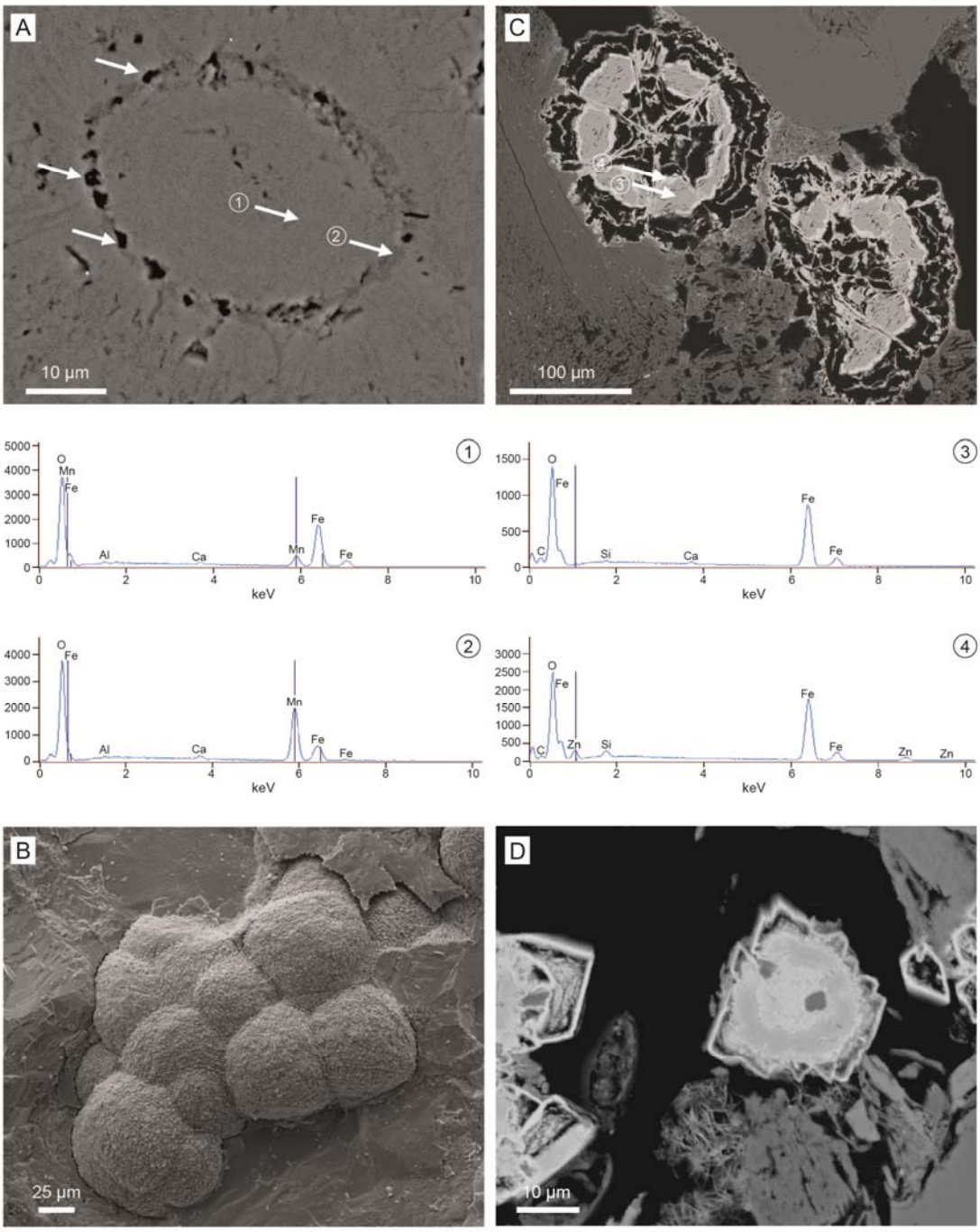

Fig. 8. Varieties of zoned sphaerosiderites

A. Rhodochrosite rim with dissolution voids marking one of the zones in sphaerosiderite. Norra Albert quarry, 516819. BSE image.

B. Cluster of rhodochrosite rimed sphaerosiderite enclosed in sparry siderite cement. Norra Albert quarry, 516819. SE image.

C. Concentric and sector zoned sphaerosiderite. Norra Albert quarry, 516820. BSE image.

D. Round siderite core covered by rhombohedral siderite. Norra Albert quarry, 516825. SE image.

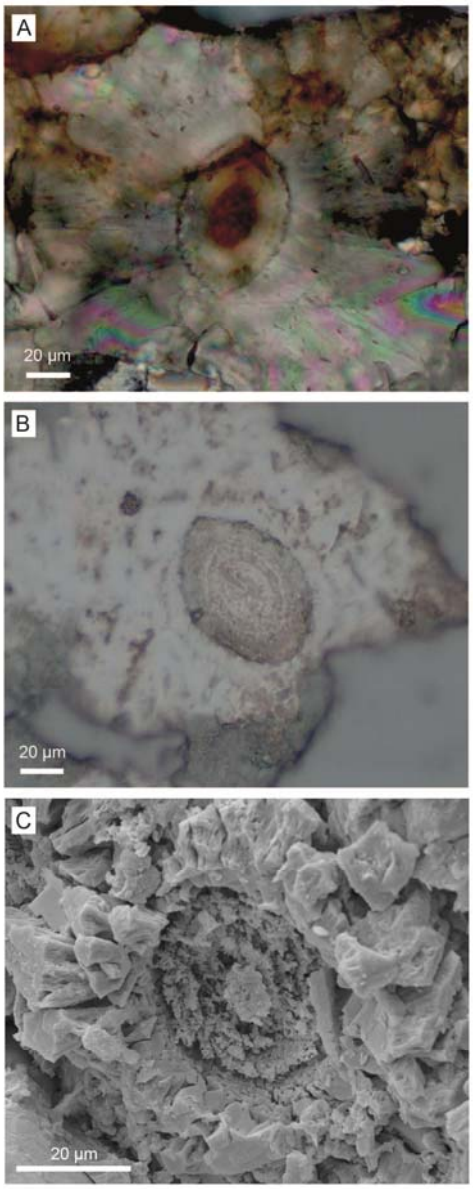

Fig. 9. Spheroidal siderite (pseudomorphs after stomata)

A. Spheroidal siderite with radiating growth around a spheroidal core and in zones. Norra Albert quarry, 516824C. Transmitted light image, crossed nicols.
B. Spheroidal siderite with marked spheroidal zones. Norra Albert quarry, 516824C. Reflected light image.
C. Spheroidal siderite with radiating growth in spheroidal zones. Acid treated sample, Norra Albert quarry, 516824C. SE image.

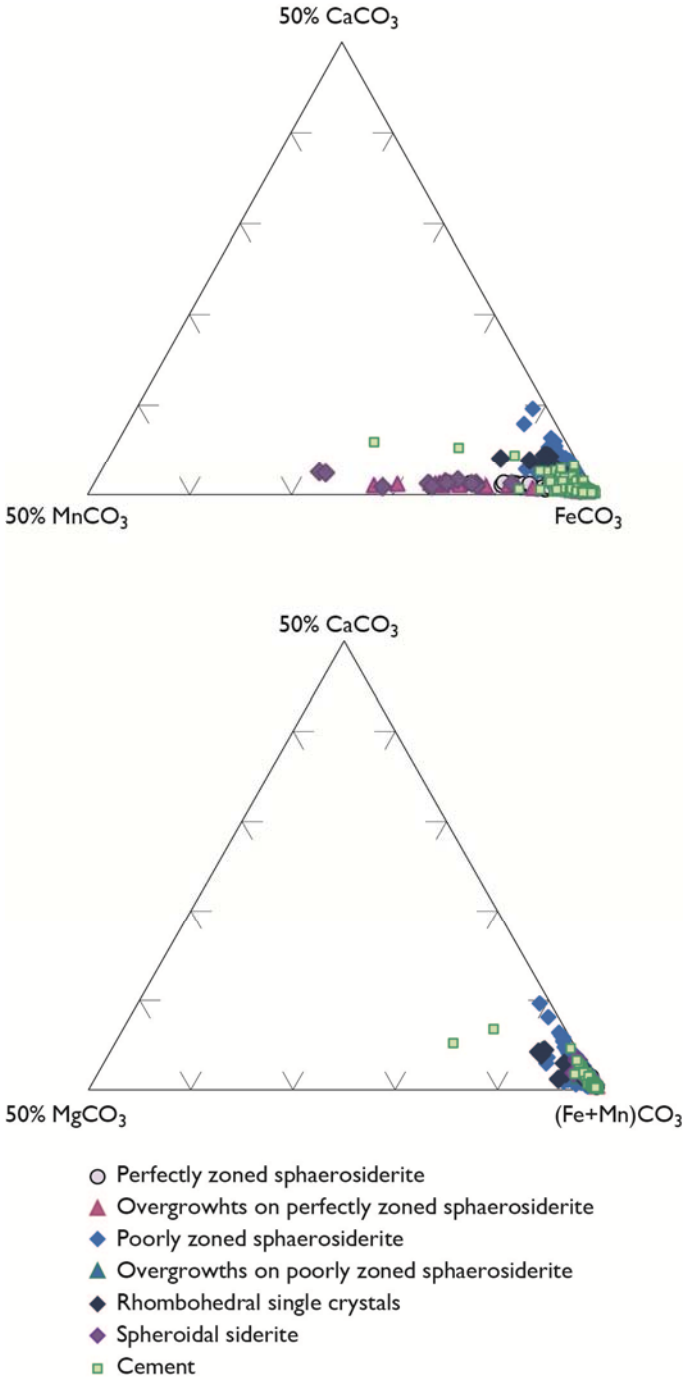

Fig. 10 Chemical composition

Microprobe analyses show that siderite generally has a low content of Mg and Ca, though occasionally relatively high content of Mn.

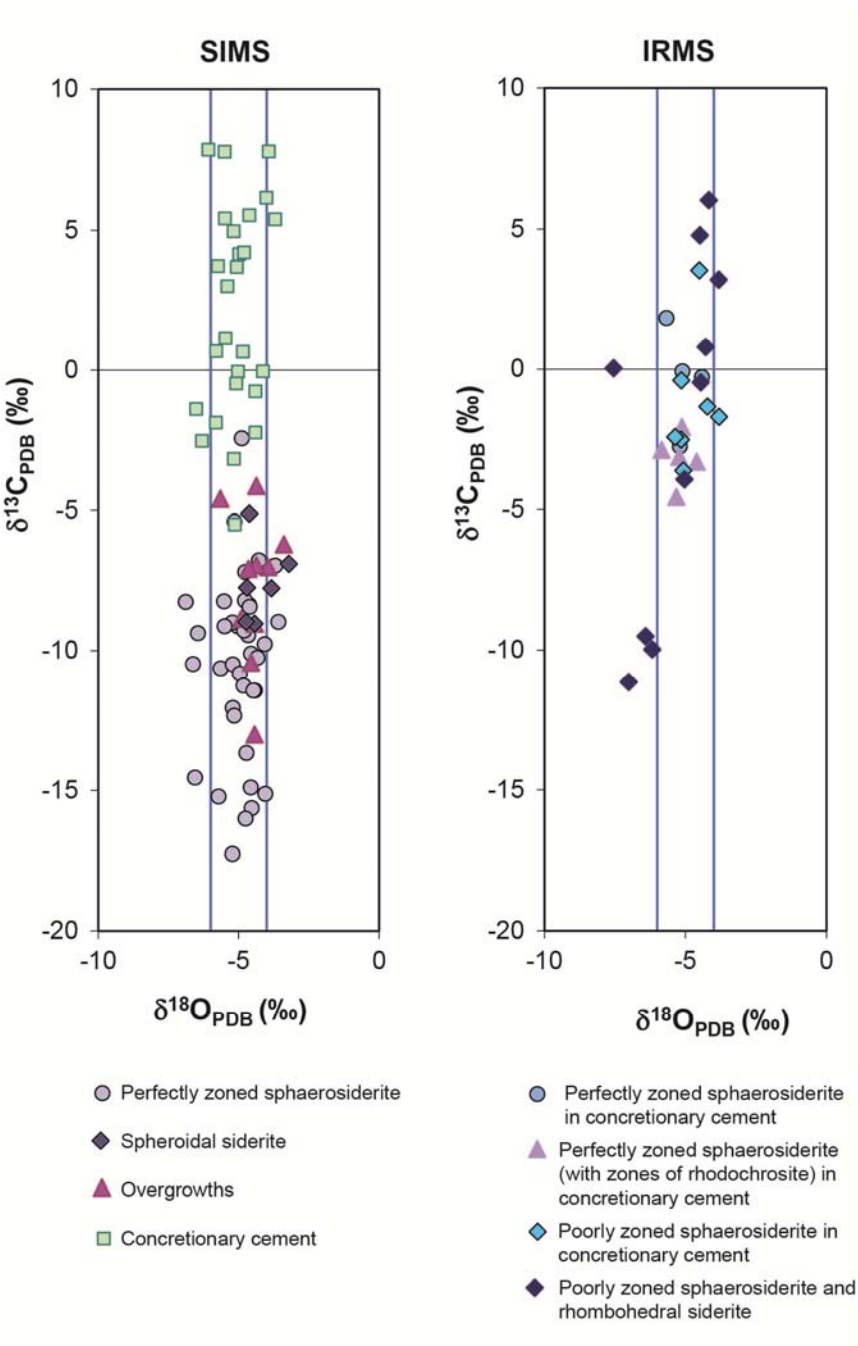

Fig. 11. Isotopic composition

The siderite isotopic composition measured by conventional mass spectrometry on bulk rock samples (bulk rock) and in specific siderite morphologies (*in situ*) by ion probe. Perfectly zoned sphaerosiderite and spheroidal siderite have similar and slightly lower $\delta^{13}C$ values than the siderite matrix. Bulk rock analyses of several samples show isotope values resembling those of *in situ* measurements of perfectly zoned sphaerosiderite, except weathered samples that have been exposed to more intensive alteration and replacement with iron-oxides/hydroxides.

Perfectly zoned sphaerosiderite

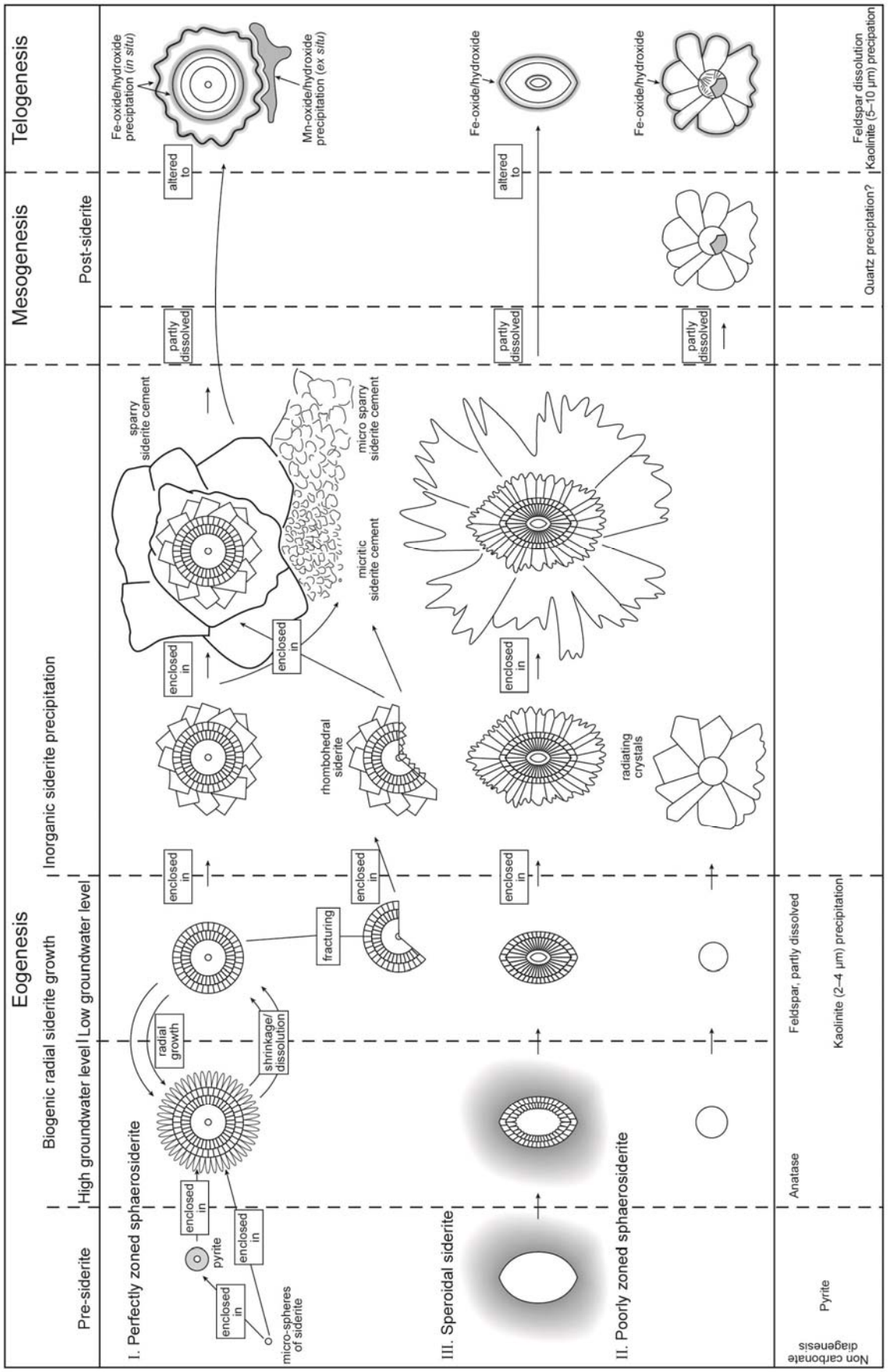

Fig. 12. Overview of siderite precipitation

Diagram showing an overview of the precipitation and growth of the different siderite morphologies in relation to other diagenetic features.